Quantifying magma overpressure beneath a submarine caldera: A mechanical modeling approach to tsunamigenic trapdoor faulting near Kita-Ioto Island, Japan

Osamu Sandanbata[1,2†], and Tatsuhiko Saito[1]

[1] National Research Institute for Earth Science and Disaster Resilience, Ibaraki, Japan.

[2] *Now at* Earthquake Research Institute, the University of Tokyo, Tokyo, Japan.

Corresponding author: Osamu Sandanbata (osm3@eri.u-tokyo.ac.jp)

Key Points (<140 characters):

- At a submarine caldera near Kita-Ioto Island, non-double-couple earthquakes with seismic magnitudes of M~5 recurred quasi-regularly.
- A mechanical model of trapdoor faulting based on a tsunami data of the 2008 event infers pre-seismic overpressure in a magma reservoir.
- The trapdoor faulting, driven by magma overpressure of ~10 MPa, partly relieved the pressure, affecting the caldera's magmatic system.

Abstract

Submarine volcano monitoring is vital for assessing volcanic hazards but challenging in remote and inaccessible environments. In the vicinity of Kita-Ioto Island, south of Japan, unusual M~5 non-double-couple volcanic earthquakes exhibited quasi-regular repetition near a submarine caldera. Following the 2008 earthquake, a distant ocean bottom pressure sensor recorded a distinct tsunami signal. In this study, we aim to find a source model of the tsunami-generating earthquake and quantify the pre-seismic magma overpressure within the caldera's magma reservoir. Based on the earthquake's atypical focal mechanism and efficient tsunami generation, we hypothesize that submarine trapdoor faulting occurred due to highly pressurized magma. To investigate this hypothesis, we establish a mechanical earthquake model that links pre-seismic magma overpressure to the size of the resulting trapdoor faulting, by considering stress interaction between a ring-fault system and a reservoir of the caldera. The model reproduces the observed tsunami waveform data. Our estimates indicate trapdoor faulting with large fault slip occurred in the critically stressed submarine caldera accommodating pre-seismic magma overpressure of ~10 MPa. The model infers that the earthquake partially reduced magma overpressure by 10–20%, indicating that the magmatic system maintained high stress levels even after the earthquake. Due to limited data, uncertainties persist, and alternative source geometries of trapdoor faulting could lead to estimate variations. These results suggest that magmatic systems beneath calderas are influenced much by intra-caldera fault systems. Monitoring and investigation of volcanic tsunamis and earthquakes help to obtain quantitative insights into submarine volcanism hidden under the ocean.

Plain Language Summary

Monitoring submarine volcanoes is essential to understand and prepare for potential volcanic hazards in/around oceans, but it's challenging because these volcanoes are located in inaccessible environments. In a submarine volcano with a caldera structure in south of Japan, unusual volcanic earthquakes took place every several years. After one of these earthquakes in 2008, a pressure sensor deployed on the sea bottom recorded a clear signal of a tsunami. By utilizing the tsunami signal from the earthquake, we attempt to measure how much magma pressure was building up beneath the volcano before the earthquake. Assuming that the earthquake happened

with sudden rupture on an intra-caldera fault system due to highly pressurized magma beneath the volcano, we develop a method to assess the built-up magma pressure through quantification of the earthquake and tsunami sizes. By applying the method, we estimate that the volcanic edifice was under a highly stressed condition before the earthquake, suggesting active magma accumulation process that has continued beneath the volcano. Signals emitted from volcanic earthquakes under oceans shed on light to the activity of poorly monitored submarine volcanoes.

1 Introduction

Investigation of the magma pressure beneath volcanoes is important for forecasting eruptions and assessing their eruption potential. The overpressure of magma, or the excess magma pressure relative to the stress in the surrounding host rock, induces diverse volcanic unrest, such as deformation, seismicity, or gas emission, potentially triggering a volcanic eruption when the pressure exceeds the strength of the host rock (Sparks, 2003). Previous studies have tried to detect signals of volcanic unrest to examine the magma pressure and/or the stress state of the host rock (Anderson et al., 2019; Gregg et al., 2018; Le Mével et al., 2016; Massa et al., 2016; Segall & Anderson, 2021). Recently, mechanics-based numerical models have been developed to establish links between magma overpressure to surface deformation observed by on-site instruments and/or satellites. These models helped to quantify the sub-surface pressure/stress state, tracking its changes over time leading up to eruptions (Cabaniss et al., 2020; Gregg et al., 2022; Segall & Anderson, 2021). Consequently, these previous studies provided quantitative insights into the eruption triggering due to the magma overpressure. Thus, magma pressure or elastic stress status in volcanoes can be vital proxies for assessing the potentials and the timings of eruptions.

Submarine volcanoes have the potential to cause disastrous eruptions sometimes with volcanic tsunamis, as highlighted by recent events like Hunga Tonga-Hunga Ha'apai, Tonga (Kubota et al., 2022; Lynett et al., 2022; Purkis et al., 2023), or Anak Krakatau, Indonesia (Grilli et al., 2019; Heidarzadeh et al., 2020; Ye et al., 2020). However, it is often challenging to investigate submarine volcanoes due to the lack of on-site monitoring systems in most cases. Many previous studies remotely detected geophysical signals from submarine volcanoes, such as, seawater acoustic waves (Metz et al., 2016; Tepp & Dziak, 2021), seismic waves (Cesca et

al., 2020; Saurel et al., 2021; Sugioka et al., 2001), or tsunami waves (Fukao et al., 2018; Sandanbata et al., 2018; Y. Wang et al., 2019), shedding light on volcanic processes in submarine volcanoes. However, only a limited number of studies have utilized these remote signals to examine the magma pressure or the stress state of submarine volcanoes.

In this paper, we aim to investigate the magma overpressure and the stress status in a submarine caldera near Kita-Ioto Island, south of Japan, by studying a volcanic earthquake driven by the sub-caldera magma accumulation. We first report volcanic earthquakes with seismic magnitudes of M_w~5 that recurred near the caldera, and show that one of the earthquakes in 2008 caused a tsunami that traveled in the ocean over a distance of ~1,000 km. We then develop a mechanical model of the earthquake to quantitatively link the sub-caldera magma overpressure to the earthquake size and thereby the tsunami size. By combining the tsunami waveform data with the mechanical model, we estimate the magma overpressure that drove the volcanic earthquake, as well as explain the tsunami generation.

2 Tsunami signal from a volcanic earthquake at Kita-Ioto submarine caldera

Kita-Ioto Island is an inhabited island in the Izu-Bonin Arc, to the northwest of which a submarine caldera with a size of 12 km x 8 km is located, hereafter called *Kita-Ioto caldera* (Figures 1a–1c). Although no historical eruption on the island has been reported, past submarine eruptions were found at a submarine vent called *Funka Asane* on a major cone within the caldera structure (Figure 1c). The latest eruptions of Funka Asane were reported between 1930 to 1945 (Japan Meteorological Agency, 2013), and its volcanic activity has been recently inferred from sea-color changes and underwater gas emission near the vent (JMA, 2013, Ossaka et al., 1994). Yet, the volcanic activity of the submarine caldera has not been understood well.

Active volcanism of Kita-Ioto caldera shows unique seismic activity characterized by shallow earthquakes near the caldera repeating every 2–5 years, in 2008, 2010, 2015, 2017, and 2019, in addition to that in 1992 (Figure 1c; Table S1). As the focal mechanism of the earthquake in 2008 represents in Figure 1c, these six earthquakes reported in the Global Centroid Moment Tensor (GCMT) catalog (Ekström et al., 2012) similarly had seismic magnitudes of M_w 5.2–5.3 and moment tensors with large compensated-linear-vector-dipole (CLVD) components in a nearly vertical tension axis (Figure S1). Such earthquakes at a shallow depth in volcanic or geothermal environments are often called vertical-CLVD earthquakes (e.g., Shuler, Nettles, &

Ekström, 2013; Sandanbata, Kanamori, et al., 2021). No eruptions were reported around the times of these earthquakes, but these earthquakes with moderate-sized seismic magnitudes indicate volcanic activity of the submarine caldera. This type of earthquakes has been explained in past studies by different source mechanisms, such as fault slips in calderas, deformation of a magma reservoir, or volume change due to heated fluid injection (Shuler, Ekström, & Nettles, 2013), but they are indistinguishable only from the seismic characters, mainly due to a tradeoff between the vertical-CLVD and isotropic components of moment tensors (Kawakatsu, 1996).

Following the earthquake that occurred at 13:10 on 12 June 2008 (UTC), a tsunami-like signal was recorded by an ocean-bottom-pressure (OBP) gauge with a sampling interval of 15 s of the station 52404, ~1,000 km away from the caldera, of Deep-ocean Assessment and Reporting of Tsunamis (DART) system (Bernard & Meinig, 2011) (Figures 1a). Figure 1d shows the OBP data, which we obtain by removing the tidal trend from and by applying the bandpass (2–10 mHz) Butterworth filter to the raw record. The OBP data demonstrates that clear oscillations with the maximum pressure of ~2 mm H_2O started ~5,000 s after the earthquake origin time. Our calculation using the Geoware TTT (Tsunami Travel Time) software estimates that the tsunami would have arrived ~5,050 s after the origin time (Figure S2), if a tsunami was generated in the center of Kita-Ioto caldera at the earthquake timing. The estimated tsunami arrival time agrees well with the timing when the oscillation starts in the OBP record (Figure 1d). Our spectrogram analysis for the OBP waveform record (Figure S3) shows that lower-frequency oscillations, starting around the estimated tsunami arrival time, are followed by higher-frequency signals. This frequency-dependent character with later arrivals of higher-frequency components is typical for tsunami waves with the dispersion that traveled over long distances (Saito et al., 2010; Sandanbata et al., 2018). Hence, it is very likely that the OBP gauge captured a tsunami signal from the 2008 earthquake at Kita-Ioto caldera.

3 Hypothetical source mechanism

Given the tsunami generation by the vertical-CLVD earthquake at Kita-Ioto caldera, hereafter we call *Kita-Ioto caldera earthquake*, the most plausible mechanism is *trapdoor faulting*, or sudden slip of an intra-caldera ring fault interacting with a sill-like magma reservoir accommodating highly pressurized magma. The trapdoor faulting was first reported in a subaerial caldera of Sierra Negra volcano in the Galapagos Islands, where the phenomenon

occurred several times with vertical-CLVD earthquakes of M_w~5 several times and caused the caldera uplift of a few meters by each event (Amelung et al., 2000; Gregg et al., 2018; Jónsson, 2009; Shreve & Delgado, 2023; Zheng et al., 2022). Recently, Sandanbata et al. (2022; 2023) revealed that trapdoor faulting repeated with M_w 5.4–5.8 vertical-CLVD earthquakes and generated large tsunamis at two submarine calderas: Sumisu caldera in the Izu-Bonin Arc (Sandanbata et al., 2022), and a submerged caldera near Curtis Island, or Curtis caldera, in the Kermadec Arc (Sandanbata et al., 2023). Those submarine earthquakes are similar to the 2008 Kita-Ioto caldera earthquake in terms of seismic and tsunami characters, and source environments in calderas, leading to our hypothesis of submarine trapdoor faulting for the Kita-Ioto caldera earthquake.

4 Methodology

In this section, we describe the methodology to construct a 3-D mechanical model of trapdoor faulting and to apply it to the tsunami data of the 2008 Kita-Ioto caldera earthquake. Through the application, we attempt to reproduce the tsunami data and estimate the sub-caldera magma overpressure that drove the tsunamigenic earthquake.

4.1 Mechanical model of trapdoor faulting

We consider the 3-D half-space elastic medium with an intra-caldera ring fault and a horizontal crack filled with magma (Figure 2). The ring fault and the horizontal crack are discretized into small triangular meshes, or sub-faults and sub-crack (with N_F and N_C meshes), respectively. The crack is assumed to have a finite inner volume and filled with compressible magma.

We assume that trapdoor faulting is driven by magma overpressure in the crack, as follows; before trapdoor faulting, continuous magma input into the crack gradually increases the inner pressure and volume, and causes elastic stress in the host rock, accumulating shear stress on the ring fault; when the shear stress on the fault overcomes its strength, trapdoor faulting takes place. In the following, we model trapdoor faulting as a dislocation model that combines sudden and interactive processes of dip-slip on the fault with stress drop, deformation (vertical opening/closure) of the crack with volume change, and pressure change of the magma in the crack. Note that, some previous studies used the terminology of trapdoor faulting to refer to only

the fault part (e.g., Amelung et al., 2000), while we consider it as the composite process involving both the fault and the magma-filled crack.

Pre-seismic elastic stress in the host rock

As a reference state, we consider that the magma pressure p_0 in the crack is in equilibrium with the background stress σ_{ij}^0 in the host rock due to the lithostatic and seawater loading, and that the background differential stress as zero. If we take the stress in the host rock as positive when it is compression, the background stress at an arbitrary position in the reference state is expressed as:

$$\sigma_{ij}^0 = p_0 \frac{z}{z_0} \delta_{ij}, \text{ — (1)}$$

where z and z_0 are the depth in the host rock and the crack depth, respectively, and δ_{ij} is the Kronecker's delta.

We assume that long-term magma input into the crack increases the magma overpressure and opens the crack vertically, and that the resultant crack deformation changes the stress in the host rock. Thus, the shear stress is accumulated on the fault, which eventually causes trapdoor faulting. Magma pressure in the pre-seismic state, just before trapdoor faulting, is assumed to be spatially uniform within the crack and expressed as $p = p_0 + p_e$, where p_e is the pre-seismic magma overpressure. If we denote the spatial distribution of the crack opening in the pre-seismic state as $\underline{\delta_e}$, the equilibrium relationship between the normal stress on the surfaces of sub-cracks and the inner magma pressure reduces to:

$$\underline{\sigma_e} = P\underline{\delta_e} = p_e \underline{I_C}, \text{ — (2)}$$

where $\underline{\sigma_e}$ is the $N_C \times 1$ column vector of the pre-seismic normal stress on sub-cracks, P is the interaction matrix, with a size of $N_C \times N_C$, that map the tensile opening of sub-cracks into the normal stress on sub-cracks, and $\underline{I_C}$ is the $N_C \times 1$ column vector of ones. The distribution of the crack opening in the pre-seismic state $\underline{\delta_e}$ can be obtained from the second equality of Equation 2. Then, the pre-seismic shear stress along the dip direction on the surfaces of sub-faults (denoted as $\underline{\tau_e}$) created by the magma overpressure p_e can be expressed as:

$$\underline{\tau_e} = Q\underline{\delta_e}, \text{ — (3)}$$

where Q is the interaction matrix, with a size of $N_F \times N_C$, that maps the tensile opening of sub-cracks into the shear stress on sub-faults. With Equation 2, Equation 3 can be rewritten as:

$$\underline{\tau_e} = p_e\left(QP^{-1}\underline{I_C}\right). \text{ — (4)}$$

The part in the bracket, $QP^{-1}\underline{I_C}$, represents the shear stress on the surfaces of sub-faults due to unit magma overpressure. If we denote it as $\underline{\hat{\tau}_e}$, Equation 4 can be rewritten as:

$$\underline{\tau_e} = p_e\underline{\hat{\tau}_e}. \text{ — (5)}$$

Occurrence of trapdoor faulting

Trapdoor faulting is caused by sudden stress drop of the shear stress accumulated on the fault. The motion involves dip-slip of the fault, and deformation (opening/closure) of the crack. To determine the motion of trapdoor faulting, we here derive two boundary conditions on the surfaces of the ring fault and the horizontal crack.

Assuming that the shear stress along the dip direction on the fault decreases by a stress drop ratio α due to trapdoor faulting, the boundary condition on the surface of the fault can be expressed as:

$$\underline{\Delta\tau} = Q\underline{\delta} + R\underline{s} = -\alpha\underline{\tau_e}, \text{ — (6)}$$

where $\underline{\Delta\tau}$ is the $N_F \times 1$ column vector of the shear stress change on sub-faults during trapdoor faulting. Q and R, with sizes of $N_F \times N_C$ and $N_F \times N_F$, map dip-slip of sub-faults into the normal stress on sub-crack and the shear stress on sub-faults, respectively (Q is the same as that in Equation 3).

Sudden stress change in the host rock due to dip-slip of the fault interactively accompanies deformation (opening/closure) of the crack, and the resultant normal stress change on the crack induces horizontal movement of the inner magma. For simplicity, we assume that the magma movement finishes and the magma pressure becomes spatially uniform in the crack quickly. Under this simplification, the boundary condition on the surface of the horizontal crack is derived from the equilibrium relationship between the normal stress on sub-cracks and the inner magma pressure, as follows:

$$\underline{\Delta\sigma} = P\underline{\delta} + U\underline{s} = (\Delta p)\underline{I_c}, \text{ — (7)}$$

where $\underline{\Delta\sigma}$ and Δp are the $N_C \times 1$ column vector of the normal stress change on sub-cracks and the scalar of the magma pressure change during trapdoor faulting, respectively. P and U are the interaction matrices, with sizes of $N_C \times N_C$ and $N_C \times N_F$, that map the tensile opening of sub-cracks into the normal stress on sub-cracks and into the shear stress on sub-faults, respectively (P is the same as that in Equation 2).

The magma pressure change Δp during trapdoor faulting can be related to the crack volume change ΔV through the mass conservation law, as follows:

$$\Delta m/\rho_m = V_0 \beta_m \Delta p + \Delta V, \text{ — (8)}$$

where Δm is the magma influx and β_m is the compressibility of magma. Since previously observed trapdoor faulting occurred within less than ~10 s (Geist et al., 2008; Sandanbata et al., 2022, 2023), we can disregard magma mass influx during trapdoor faulting to reduce Equation 8 to:

$$\Delta p = -\frac{1}{\beta_m V_0}\Delta V = -\frac{1}{\beta_m V_0}\underline{A}^T\underline{\delta} = -\frac{1}{\beta_m V_0}\sum_{k=1}^{N_c} A_k \delta_k, \text{ — (9)}$$

where $\underline{A}$ is the $N_C \times 1$ column vector of the areas of sub-cracks.

By substituting Equations 5 and 9 into Equations 6 and 7, respectively, we obtain the following equations:

$$\begin{bmatrix} P & U \\ Q & R \end{bmatrix}\begin{bmatrix} \underline{\delta} \\ \underline{s} \end{bmatrix} = \begin{bmatrix} \left(-\frac{1}{\beta_m V_0}\underline{A}^T\underline{\delta}\right)\underline{I_C} \\ -\alpha p_e \underline{\hat{\tau}_e} \end{bmatrix}. \text{ — (10)}$$

Equation 10 can be rewritten by:

$$\begin{bmatrix} P' & U \\ Q & R \end{bmatrix}\begin{bmatrix} \underline{\delta} \\ \underline{s} \end{bmatrix} = p_e \begin{bmatrix} \underline{0} \\ -\alpha\underline{\hat{\tau}_e} \end{bmatrix}, \text{ — (11)}$$

where

$$P' = P + \frac{1}{\beta_m V_0}\underline{A}^T \text{ (or } P'_{ij} = P_{ij} + \frac{1}{\beta_m V_0}A_j). \text{ — (12)}$$

Equations 11 and 12 represent $N_C + N_F$ equations with $N_C + N_F$ unknown values ($\underline{\delta}$, $\underline{s}$), if we priorly assume the pre-seismic magma overpressure p_e, the stress drop ratio α, the source geometry determining the interaction matrices, and the parameters β_m and V_0. In this study, the

source geometry and the parameters are assumed as described in Section 4.2. Also, the stress drop ratio is simply assumed as $\alpha = 1$; in other words, the pre-seismic shear stress on the fault completely vanishes to zero due to trapdoor faulting. In this case, Equation 11 is reduced to:

$$\begin{bmatrix} P' & U \\ Q & R \end{bmatrix} \begin{bmatrix} \underline{\delta} \\ \underline{s} \end{bmatrix} = p_e \begin{bmatrix} \underline{0} \\ -\underline{\hat{\tau}_e} \end{bmatrix}, \quad \text{— (13)}$$

By solving Equation 13 with Equation 12 for ($\underline{\delta}$, $\underline{s}$), we can determine the motion of trapdoor faulting generated by pre-seismic magma overpressure p_e. Also, we can estimate the co-seismic changes of magma pressure and crack volume due to trapdoor faulting by substituting $\underline{\delta}$ into Equation 9, and the stress drop by substituting $\underline{s}$ into Equation 6.

4.2 Model setting

The source geometry employed for main results is shown in Figure 2. A partial ring fault is along an ellipse with a size of 3.6 km × 2.6 km on seafloor; the center is at (141.228°E, 25.4575°N), and its major axis is oriented N60°E. The fault is on the NW side of Kita-Ioto caldera with an arc length of 90° and dips inwardly with a dip angle of 83°; this fault setting on the NW side is based on our moment tensor analysis that suggests a ring fault orientated in the NE–SW direction (see Text S1, for details). The fault traces several small cones found on the NW side of the caldera floor (Figure 1c), given that cone structures are often formed over a sub-caldera ring fault (Cole et al., 2005). The fault's down-dip end connects to a horizontal crack at a depth of 2 km. The crack is elliptical in shape, 15% larger than the size of an ellipse traced along the fault's down-dip end. After discretizing the source geometry into sub-faults and sub-cracks, the four interaction matrices (*P*, *Q*, *R*, and *U*) between sub-faults and sub-cracks are computed by the triangular dislocation (TD) method (Nikkhoo & Walter, 2015), when we assume the Poisson's ratio of 0.25 and the Lame's constants λ and μ of 5 GPa.

The product $V_0\beta_m$ controls how the magma-filled crack responds to stress perturbation by faulting, as explained by Zheng et al. (2022). For main results, we assume the crack volume V_0 and the magma compressibility β_m as 1.5 x 10^{10} m^3 (corresponding to a crack thickness of ~500 m) and 1.0 x 10^{-10} Pa^{-1} (from a typical value for degassed basaltic magma [e.g., Kilbride et al., 2016]), respectively, thereby, $V_0\beta_m$ = 1.5 m^3/Pa. This product value is similar to Zheng et al.'s (2022) estimates for a magma reservoir of Sierra Negra caldera.

4.3 Constraint from the tsunami data of the 2008 Kita-Ioto caldera earthquake

We apply the mechanical model of trapdoor faulting to the tsunami data of the 2008 Kita-Ioto caldera earthquake. Utilizing the linear relationship between ($\underline{\delta}$, $\underline{s}$) and p_e through Equation 13, we estimate the pre-seismic magma overpressure p_e causing the earthquake by constraining the magnitude of trapdoor faulting from the tsunami data.

For estimation of p_e, we prepare a model of trapdoor faulting due to unit pre-seismic magma overpressure p_e = 1 Pa, which we call unit-overpressure model, and then simulate a tsunami OBP waveform at the station 52404 from the model (see the methodology in Section 4.4). We denote the synthetic waveform as $\underline{\hat{m}}$ and consider it as the tsunami OBP amplitude due to unit overpressure, whose unit is [mm H_2O/Pa]. Because of the linearity of the tsunami propagation problem we employ, the amplitude of tsunami waveform is linearly related to the magnitude of trapdoor faulting, and thereby to the pre-seismic magma overpressure p_e through Equation 13. Therefore, the synthetic tsunami waveform from trapdoor faulting due to an arbitrary p_e can be expressed as $\underline{m} = p_e\underline{\hat{m}}$. Supposing that the tsunami signal from the 2008 earthquake recorded in the OBP data (denoted by $\underline{d}$) is reproduced well by $\underline{m}$, we can estimate the pre-seismic magma overpressure p_e from:

$$p_e = \frac{\rho_d}{\hat{\rho}}, \quad \text{— (14)}$$

where ρ_d and $\hat{\rho}$ are the root-mean-square (RMS) amplitudes of $\underline{d}$ and $\underline{\hat{m}}$ (in units of [mm H_2O] and [mm H_2O/Pa]), respectively. The time window for calculating the RMS amplitudes is set as it includes major oscillations in earlier parts of the observed waveform (Figure 1d).

4.4 Tsunami waveform simulation

A tsunami waveform from the unit-overpressure model $\underline{\hat{m}}$ is synthesized as follows. Assuming ($\underline{\delta}$, $\underline{s}$) of the unit-overpressure model, we compute the vertical seafloor displacement by the TD method, and convert it to vertical sea-surface displacement by applying the Kajiura filter (Kajiura, 1963). We then simulate the tsunami propagation from the sea-surface displacement over Kita-Ioto caldera, by solving the linear Boussinesq-type equations in the finite-difference scheme of the JAGURS code (Baba et al., 2015). The outputted 2-D maps of sea-surface wave heights, every 5 s, are converted into maps of OBP perturbation by

303 incorporating reduction of tsunami pressure perturbation with increasing water depth (e.g.,
304 Chikasada, 2019). The synthetic waveform of OBP perturbation at the station 52404 is obtained
305 from the OBP maps. We use a phase correction method for short-period tsunamis (Sandanbata,
306 Watada, et al., 2021) to improve the synthetic waveform accuracy by incorporating a theoretical
307 tsunami dispersion, including effects of the elastic Earth and the seawater compressibility during
308 long-distance propagation.

309 **5 Results**

310 5.1 Source model of the 2008 Kita-Ioto caldera earthquake

311 Under the model setting explained in Section 4.2, we obtain a trapdoor faulting model for
312 the 2008 Kita-Ioto caldera earthquake that explains the OBP tsunami data (Figure 3). The pre-
313 seismic magma overpressure p_e constrained from the OBP tsunami data is 11.8 MPa. Figures 3b
314 and 3c show the spatial distributions of the ring-fault slip $\underline{s}$ and the crack opening/closing $\underline{\delta}$
315 during trapdoor faulting. Large reverse slip at maximum of 8.9 m is on the ring fault, near which
316 the inner crack opens by 5.5 m at maximum and the outer closes by 2.7 m. In the SE area, the
317 crack closes broadly with a maximum value of 0.86 m. In total, the crack volume increases by
318 ΔV = 0.0030 km^3. The co-seismic magma pressure change Δp is –1.97 MPa during trapdoor
319 faulting, meaning that the magma overpressure drops by 16.7 % relative to the pre-seismic state
320 and makes additional storage for magma. The response of the magmatic system to faulting may
321 have postponed eruption timing; on the other hand, post-seismic magma overpressure is
322 estimated to remain at a high level (~9.8 MPa) even after trapdoor faulting.

323 The obtained trapdoor faulting model is predicted to cause large asymmetric caldera-floor
324 uplift, thereby generating a tsunami efficiently. The large seafloor displacement is concentrated
325 near the fault, with the maximum uplift of as large as 5.6 m and outer subsidence of 2.8 m
326 (Figure 3d). The sea surface displacement is smoothed by the low-pass effect of seawater,
327 resulting in seawater uplift of 3.6 m within the caldera rim with the exterior subsidence of 1.1 m
328 (Figure 3e). Figure 3f compares the synthetic tsunami waveform from the model with the OBP
329 tsunami signal recorded at the station 52404, which demonstrates good waveform agreement,
330 including later phases that are not used for the amplitude fitting. In addition, the spectrogram
331 analysis confirms quite similar tsunami travel times and dispersive properties of the two

waveforms (Figures 3g and 3h). These results support the reasonability of our mechanical model for the 2008 Kita-Ioto caldera earthquake.

5.2 Pre-seismic state just before trapdoor faulting

From the mechanical model, we consider how trapdoor faulting is caused by the inflated crack. In the pre-seismic state just before trapdoor faulting, the crack has inflated with vertical opening $\underline{\delta_e}$ of 12.1 m at maximum due to the pre-seismic magma overpressure p_e (Figure 4a). The inner volume has been increased by 0.21 km^3 relative to that in the reference state. This pre-seismic crack opening generates the shear stress on the fault $\underline{\tau_e}$, which takes its maximum value of 11.6 MPa (Figures 4b); this value corresponds to the stress drop during trapdoor faulting, because we assume that the stress totally vanishes co-seismically.

In a simple earthquake paradigm of the stick-slip motion, which assumes that slip occurs when the shear stress overcomes the static frictional stress (e.g., pp. 14 of Udias et al., 2014), the fault requires friction to remain stationarity until just before faulting occurrence. The total normal stress on the fault $\underline{\sigma_0^F}$ is the sum of the effects of the crack opening $\underline{\sigma_e^F}$ (Figure 4c) and the lithostatic and seawater loading $\underline{\sigma_{lit}^F} + \underline{\sigma_{sea}^F}$, as shown in Figure 4d (see the caption). By taking a ratio of the area-averaged values of $\underline{\tau_e}$ and $\underline{\sigma_e^F}$, the static friction coefficient on the ring fault can be estimated as 0.31. The frictional fault system may enable the caldera system to accommodate the high magma overpressure without fault slip until trapdoor faulting. Note that, however, sophisticated modeling approaches including realistic fault friction law will be needed for investigation of the dynamic initiation process.

5.3 Deformation and elastic stress change in the host rock

Our model demonstrates how trapdoor faulting deforms the host rock and changes its elastic stress. With the model outputs, we compute the displacement, stress and strain fields in the host rock along an SE-NW profile across the caldera (see a dashed line in Figure 3c) by the TD method; the pre-seismic state is from $\underline{\delta_e}$, the co-seismic change is from ($\underline{\delta}$, $\underline{s}$), and the post-seismic state is the sum of the pre-seismic state and the co-seismic change. We also calculate the shear-strain energy from the stress and strain fields (e.g., Saito et al., 2018). When we denote the stress tensors in the host rock as:

$$\tau_{ij} = \tau'_{ij} + \frac{1}{3}\tau_{kk}\delta_{ij}, \quad (15)$$

where τ'_{ij} is the deviatoric components, δ_{ij} is the Kronecker's delta, the shear-strain energy density W in the elastic medium can be expressed as:

$$W = \frac{1}{4\mu}\tau'_{ij}\tau'_{ij}. \quad (16)$$

Note that the shear-strain energy density is zero in the reference state ($p = p_0$), where the deviatoric stress is assumed to be zero. Using Equation 16, the shear-strain energy density in the pre- and post-seismic states, W^{pre} and W^{post}, can be calculated with the deviatoric shear stress. The co-seismic change in the shear-strain energy density is obtained by:

$$\Delta W = W^{post} - W^{pre}. \quad (17)$$

Figures 5a–5c show displacement in the host rock along the SE–NW profile. In the pre-seismic state (Figure 5a), since the fault accommodates no slip, the host rock deforms purely elastically from the reference state due to the opening crack and causes large uplift of the caldera surface by 8.8 m at maximum at the caldera center. During trapdoor faulting, the co-seismic displacement is concentrated along the fault (Figure 5b). The inner caldera block uplifts by 5.7 m at maximum, while the outer host rock moves downward by 3.2 m. The fault motion accompanies crack opening beneath the NE side of the caldera block, whereas slight downward motion is seen in the SE part of the caldera block, which can be attributed to elastic response to magma depressurization. Figure 5c shows the displacement in the post-seismic state, where the upward displacement is confined within the caldera block with cumulative uplift of 9.9 m at maximum from the center to near the fault, while notable deformation is not found outside the fault. As shown in Figure 5d, the pre-seismic seafloor displacement takes its uplift peak in the center, while after trapdoor faulting the seafloor becomes almost flat on the NW side near the fault. This indicates that if we take a long term including the pre-seismic inflation and trapdoor faulting, the caldera causes a block-like motion with a clear boundary cut by the fault.

In terms of the stress and the shear-strain energy, trapdoor faulting can be considered as a process that releases the shear-strain energy accumulated in the host rock. Figures 5e–5g show the shear-strain energy density with the principal axes of the stress field in the host rock along the same SE–NW profile. In the pre-seismic state, the shear-strain energy density is concentrated around the crack edge, or near the fault (Figure 5e). The plunge of the maximum compressional

389 stress near the fault ranges from ~50° in the middle of the fault, which preferably induces a
390 reverse slip on a steeply dipping fault. During trapdoor faulting (Figure 5f), the shear-strain
391 energy density near the fault on the NW side dramatically decreases, and it is slightly reduced
392 even on the SE side in response to co-seismic magma depressurization. Eventually, in the post-
393 seismic state (Figure 5g), the shear-strain energy density almost vanishes near the fault.

394 **6 Discussion**

395 6.1 Model uncertainties

396 Our source model has been constructed in the model setting as described in Section 4.2.
397 However, we do not have enough data to constrain the sub-surface structure and magma
398 property, so that our model outputs vary depending on how the model setting is assumed priorly.

399 6.1.1 Depth of a horizontal crack

400 The depth of a horizontal crack, or a magma reservoir, influences much our pre-seismic
401 magma overpressure estimation. When a deeper crack is assumed at a depth of 4 km below
402 seafloor (Figure 6), the estimated magma overpressure p_e is 22.26 MPa, almost twice larger
403 compared to our main result assuming a depth of 2 km (Figure 3). The obtained model with a 4-
404 km deep crack explains the tsunami data well, even better than that with a 2-km deep crack
405 (compare waveforms and spectrograms in Figures 3f–3h and 6f–6h), implying preference of the
406 deeper crack model. When a crack is located deeper in the crust, the magnitude of the crack
407 opening per unit magma overpressure becomes smaller because it is farther from the free-surface
408 seafloor (Fukao et al., 2018). This lowers the shear stress on the fault generated per unit magma
409 overpressure, and thereby larger pre-seismic magma overpressure is required to cause a similar-
410 sized earthquake and tsunami. Despite the large difference in pre-seismic magma overpressure,
411 the estimated co-seismic parameters for the 2008 earthquake, such as magnitudes of fault slips,
412 crack deformation, and changes in magma pressure and crack volume, do not change largely.

413 6.1.2 Arc length of a ring fault

414 The arc length of a ring fault is also an important factor affecting our modeling. As
415 shown in Figure 7, when we assume a ring fault with an arc length of 180°, or a half-ring fault,
416 on the NW side, pre-seismic magma overpressure p_e is estimated as 4.84 MPa, less than half of

the output from our main results assuming an arc length of 90° (Figure 3). This large difference can be attributed to two main causes. First, the average fault slip amount is known to be proportional to the faut length when the stress drop is identical (Eshelby, 1957); therefore, a longer ring fault causes large slip efficiently, compared to that on a shorter arc length. Additionally, trapdoor faulting with a longer fault uplifts larger volume of seawater over a broader area (compare Figures 7e and 3e), making its tsunami generation efficiency higher.

Although smaller magma overpressure (p_e = 4.84 MPa) is estimated in the case with a ring-fault arc angle of 180°, we emphasize that the co-seismic magma pressure change Δp is as large as –1.99 MPa. The magma overpressure efficiently drops by 41.1 % from the pre-seismic state, in contrast to the ratio of only 16.7 % in the case of an arc length of 90° (see Section 5.1). The difference arises from the fact that the fault slip along a longer segment can induce the crack opening in a broader area and increase the inner volume more, resulting in more efficient pressure drop. The two models with different ring-fault arc lengths produce very similar tsunami waveforms at the station 52404 (compare Figures 7f and 3f), indicating the difficulty in distinguishing the arc length from our dataset. However, these results provide an important insight that the magma pressure drop ratio strongly depends on a fault length ruptured during trapdoor faulting, suggesting importance to investigate the intra-caldera fault geometry for robust quantification of magma pressure change due to trapdoor faulting.

6.1.3 Other uncertainties

We discuss on effects of the product $V_0\beta_m$, which controls how the magma-filled crack responds to stress perturbation by faulting. The effects in extreme cases are discussed by Zheng et al. (2022); when $V_0\beta_m \to 0$, the crack involves no total volume change ($\Delta V \to 0$), while a magnitude of magma pressure drop becomes the largest; on the other hand, when $V_0\beta_m \to \infty$, the net volume change of the crack is at maximum, while no pressure change occurs ($\Delta p \to 0$). In previous studies of the 2018 Kilauea caldera collapse and eruption sequence, the estimated product ranges 1.3–5.5 m^3/Pa (Anderson et al., 2019; Segall & Anderson, 2021). We assumed $V_0\beta_m$ = 1.5 m^3/Pa for our main results, which is close to the lower end of the range. To examine the model variations, we try the source modeling alternatively by assuming $V_0\beta_m$ = 6.0 m^3/Pa, near the upper limit of the range estimated in the case of Kilauea. For the larger $V_0\beta_m$, the area of the crack opening becomes broader, while a magnitude of the closure on the other side becomes

smaller (Figures S4a–S4c; compare them with Figures 3a–3c). The sea-surface displacement is thereby broader (Figure S4e), exciting long-period tsunamis more efficiently that arrives as earlier waveform phases used for the amplitude fitting (Figure S4f). Thus, in this case, our estimation of the pre-seismic magma overpressure, p_e = 9.11 MPa, becomes slightly smaller than the main result (p_e = 11.8 MPa); on the other hand, we estimate smaller magma pressure drop (Δp = –1.27 MPa) and a larger crack volume increase (ΔV = 0.0076 km^3). These suggest that if we take a plausible range of $V_0\beta_m$, variations of our estimations are insignificant.

It is uncertain on which side of the caldera the ruptured fault is located. Based on our moment tensor analysis (Text S1), the fault ruptured during the 2008 earthquake can be estimated to be oriented manly in the NE–SW direction, allowing us to assume two different fault locations, either of the NW or SE sides of the caldera; for our main results, we chose the model with a fault on the NW side. Here, we alternatively assume a fault on the SE side to obtain another source model to estimate the pre-seismic magma overpressure p_e as 15.36 MPa (Figure S5). Despite the fault location difference, the tsunami data is explained well by the model with a SE-sided fault (Figure S5f). The change of the estimated magma overpressure can be attributed to effects of tsunami directivity and complex bathymetry in the source region on the wave amplitude of a tsunami arriving at the station. Thus, our limited dataset is not sufficient to determine well the fault location, but the uncertainty in fault location influences our estimations insignificantly.

6.2 Comparison with previous studies

Our quantification of pre-seismic magma overpressure before trapdoor faulting in Kita-Ioto caldera (p_e = 4–22 MPa) is of the same order of magnitude as those estimated geodetically for the subaerial caldera of Sierra Negra. Gregg et al. (2018) applied a thermomechanical finite element method (FEM) model to long-term geodetic data and estimated that magma overpressure of ~10 MPa in the sill-like reservoir induced a trapdoor faulting event that occurred ~3 hours before the eruption starting on 22 October 2005. Another trapdoor faulting event on 25 June 2018 (M_w 5.4) also preceded the 2018 eruption of Sierra Negra by ten hours; Gregg et al. (2022) employed the thermomechanical FEM approach to the long-term deformation and suggested that a similar magma overpressure <~15 MPa had been accumulated to cause the failure of the trapdoor fault system.

Zheng et al. (2022), on the other hand, quantified co-seismic magma pressure change by trapdoor faulting with an m_b 4.6 earthquake on 16 April 2005. By modeling the interaction between the intra-caldera fault system and the sill-like reservoir, Zheng et al. geodetically estimated the trapdoor faulting event with a maximum fault slip of 2.1 m reduced magma overpressure by 0.8 MPa; the slightly smaller pressure change, relative to our estimation ($|\Delta p|$ = 1–3 MPa) for the 2008 Kita-Ioto earthquake, may be explained by the discrepancy in earthquake size.

Sandanbata et al. (2023) compiled the seismic magnitude and the maximum fault slip of trapdoor faulting events and demonstrated their atypical earthquake scaling relationship; in other words, trapdoor faulting accompanies larger fault slip by an order of magnitude than those for similar-sized tectonic earthquakes. Source models presented in this study for the 2008 Kita-Ioto caldera earthquake also accommodate large fault slip ranging 5–10 m at maximum, which are clearly larger those empirically predicted for M_W 5.3 tectonic earthquakes; for example, the empirical maximum slip for M_w 5.3 earthquake is only ~0.1 m, following Wells & Coppersmith (1994). This indicates the efficiency of intra-caldera fault systems in causing large slip, possibly due to their interaction with magma reservoirs (Sandanbata et al., 2022).

6.3 Long-period seismic waveforms

For validation from a different perspective, we consider long-period seismic excitation by the mechanical source model that we have obtained based on the tsunami data. For this analysis, we follow the methodology used in Sandanbata et al. (2022; 2023), as the detailed procedures are described in Text S2. We here briefly summarize the method. We first approximate the trapdoor faulting model (Figure 3) as a point-source moment tensor $\boldsymbol{M}_T$ by summing up partial moment tensors of the ring fault $\boldsymbol{M}_R$ and the horizontal crack $\boldsymbol{M}_C$ (Figure 8a–8c). We then compute long-period (80–200 s) seismic waveforms from the moment tensor $\boldsymbol{M}_T$ by using the W-phase package (Duputel et al., 2012; Hayes et al., 2009; Kanamori & Rivera, 2008) and compare the synthetic waveforms with broad-band seismic data from F-net and global seismic networks. In Figure 8d, we show synthetic seismic waveforms from the moment tensor (Figure 8a), which reproduce well the observed seismograms. This supports that our trapdoor faulting model is plausible in terms of seismic excitation, as well as tsunami generation.

We note that the moment tensor obtained from our model (Figure 8a) is much different from the GCMT solution; our model has a seismic magnitude (M_w 5.6) and is characterized by large double-couple and isotropic components, while the GCMT solution is with a smaller magnitude M_w 5.3 and a dominant vertical-T CLVD component (Figure 1d). These big differences can be attributed to very inefficient excitation of long-period seismic waves by specific types of shallow earthquake sources: a vertical opening/closing of a horizontal crack, and a double-couple source representing vertical dip-slip motion (i.e., $M_{r\theta}$ and $M_{r\phi}$ components) (Fukao et al., 2018; Sandanbata, Kanamori, et al., 2021). Since these specific sources cannot be constrained from long-period seismic waves, the GCMT solution can capture only limited parts of the source, and therefore represents a dominant vertical-T CLVD focal mechanism. These characteristic properties of long-period seismic waves from trapdoor faulting at shallow depth are discussed in more details by Sandanbata et al. (2022).

6.4 Tsunami generation by other Kita-Ioto caldera earthquakes

We have conducted a survey of OBP data from the station 52404 to determine if there were any tsunami signals following the Kita-Ioto caldera earthquakes (Figure S1), apart from that in 2008. Available data was found only for the event on 15 December 2015 (Figure 9a), for which a clear tsunami signal was recorded in the OBP data with a 15-s sampling interval (Figure 9b). However, On the other hand, we were unable to obtain OBP data to confirm tsunami signals from the earthquakes in 1992, 2010, 2017, and 2019. The station 52404 had not been deployed yet as of the 1992 event. For the other events, the bottom pressure recorders have been lost, preventing our access to its 15-s sampling-interval data. Although low-sampling data (15-min interval) sent via a satellite transfer are available, they are not useful for confirming tsunami signals with dominant periods of 100–500 s.

We further investigate the tsunami signal from the 2015 earthquake in comparison with that from the 2008 event. Note that the station location (20.7722N°, 132.3375E°) as of 2008 had shifted about 20 km northward to a new location (20.9478N°, 132.3122E°) as of 2015. To examine the similarity between the two earthquake events, we simulate a tsunami waveform at the station location as of the 2015 event from a model similar to that of the 2008 event. We assume the model setting with a deeper crack at a depth of 4 km, based on that presented in Section 6.1.1 (Figure 7). Since the GCMT catalog reports a smaller seismic moment for the 2015

event (M_0^{2015} = 8.1 × 10^{17} Nm) than that for the 2008 event (M_0^{2008} = 1.1 × 10^{18} Nm), we adjust the source model assuming a smaller pre-seismic overpressure of p_e = 16.41 MPa (= 22.26 MPa × $\frac{M_0^{2015}}{M_0^{2008}}$).

Although the observed tsunami waveforms from the two earthquakes look different (compare the waveforms in Figures 7f and 9b), the trapdoor faulting model, based on the tsunami data form the 2008 earthquake, also explains that from the 2015 earthquake overall (Figure 9), simply by changing the station location. The nonnegligible waveform difference at the two nearby locations can be attributed to the focusing/defocusing effect by complex bathymetry along the path (Figure S6; see the figure caption for details). This suggests that the 2015 earthquake was caused by trapdoor faulting, in a similar way to the 2008 earthquake. The similarity is further supported by our moment tensor analysis (see Text S1). Thus, we confirmed tsunami signals from both of the two events. Therefore, we propose that the quasi-regularly repeating earthquakes with similar magnitudes and vertical-CLVD characters reflect the recurrence of trapdoor faulting in Kita-Ioto caldera, as observed in the three calderas of Sierra Negra, Sumisu, and Curtis, where trapdoor faulting events have recurred (Bell et al., 2021; Jónsson, 2009; Sandanbata et al., 2022, 2023).

6.5 Limitations of our mechanical trapdoor faulting model

Our mechanical model of trapdoor faulting has been developed under some simplifications to focus on the essential mechanics. In this subsection we discuss some factors simplified or ignored in our model, which may influence our results.

6.5.1. Stress drop ratio

The stress drop ratio during earthquakes has been controversial in general. Some studies reported complete or near-complete stress drop during tectonic earthquakes (Hasegawa et al., 2011; Ross et al., 2017), while the stress drop ratio can be partial and vary from earthquake to earthquake (Hardebeck & Okada, 2018). For intra-caldera earthquakes, several recent studies estimated stress drop during caldera collapses (Moyer et al., 2020; T. A. Wang et al., 2022), but our knowledge on the stress drop ratio in calderas is poor and the ratio may vary from caldera to caldera.

564 We have avoided the problem by simply assuming the complete stress drop as an extreme
565 case (Equation 13, obtained by assuming $\alpha = 1$ in Equation 11); this assumption can influence
566 our estimation of the pre-seismic magma overpressure p_e. Because $\underline{s}$ and $\underline{\delta}$ are determined by the
567 stress drop on the fault, not directly by pre-seismic magma overpressure (Equation 2), if a partial
568 stress drop ratio α ($0 < \alpha < 1$) is instead assumed in Equation 11, the trapdoor faulting size due
569 to the same pre-seismic magma overpressure becomes smaller proportionally to α, and the
570 tsunami amplitude does. In this case, larger magma overpressure by a factor of $1/\alpha$ is required to
571 explain the observed tsunami amplitude. Hence, the complete stress drop assumption provides
572 lower-limit estimation of pre-seismic magma overpressure in the model setting. On the other
573 hand, estimations of co-seismic parameters, such as fault slip $\underline{s}$ and crack opening $\underline{\delta}$, and changes
574 of magma pressure Δp and crack volume ΔV, do not change regardless of our assumption of the
575 stress drop ratio α, since they are constrained form the tsunami amplitude.

576 6.5.2. Pre-slips and earthquake cycles

577 We have attributed the shear stress that generates trapdoor faulting to an inflating crack
578 alone and neglected other factors that may also cause the stress on the fault. First, different
579 segments of the intra-caldera ring fault may have caused microseismic or aseismic slips prior to
580 the occurrence of M_w~5 trapdoor faulting. In Sierra Negra caldera, high microseismicity was
581 observed along the western segment of the intra-caldera fault, leading to trapdoor faulting on the
582 southern segment before eruption (Bell et al., 2021; Shreve & Delgado, 2023). Similarly, during
583 the 2018 eruption and summit caldera collapse sequence of Kilauea, large collapse events
584 accompanying M_w~5 earthquakes were located on the southeastern and northwestern sides of the
585 summit caldera, while high microseismicity was found on other segments (Lai et al., 2021;
586 Shelly & Thelen, 2019). T. A. Wang et al. (2023) further suggested non-negligible effects on
587 large collapses of Kilauea by intra-caldera fault creep in the inter-collapse period. Such high
588 microseismicity or creeping on other fault segments, in adjacent to the ruptured segment of
589 trapdoor faulting, may impose additional shear stress.

590 Additionally, the recurrency of trapdoor faulting can play an important role in the stress
591 accumulation on the fault. Similar earthquakes have been repeated near Kita-Ioto caldera (Figure
592 S1), strongly suggesting recurrence of trapdoor faulting, as supported by the tsunami signal from
593 the 2015 earthquake (see Section 6.4). If a similar earthquake repeated on the same segment of

the fault and the stress drop is only partial, the remaining stress may influence subsequent trapdoor faulting events. Also, assuming that the earthquakes occur on different segments of the ring fault, an event on a segment increases the shear stress on its adjacent segment. Thus, in presence of additional shear stress by pre-slips or creeping on different segments or previous trapdoor faulting events, the ring fault may be ruptured by smaller pre-seismic magma overpressure. For better understanding of the physics of trapdoor faulting, further studies of the earthquake cycle in calderas are crucial.

6.5.3. Other factors

Other factors simplified in our model, such as magma reservoir geometry or rheological property of the host rock, may influence the mechanics of trapdoor faulting. While we have modeled a magma reservoir simply as an infinitely thin crack that lies horizontally, the reservoir should have a finite thickness and the geometry may not be flat, as estimated for that beneath Sierra Negra caldera (Gregg et al., 2022). The host rock has been also simplified as a homogeneous elastic medium, but the viscoelastic effects and thermal dependency of the rheological property may impact the deformation and strain states in the host rock (Cabaniss et al., 2020; Zhan & Gregg, 2019). These factors can be more important in the stress accumulation process, particularly during a long-term caldera inflation.

7 Conclusions

We have presented a new mechanical model of trapdoor faulting that quantitatively links pre-seismic magma overpressure in a sill-like reservoir and the size of trapdoor faulting. We applied this model to a tsunami-generating submarine earthquake in 2008 around Kita-Ioto caldera, for quantifying the caldera's mechanical states. Our trapdoor faulting model explains well the tsunami signal recorded by a single distant ocean bottom pressure gauge, as well as regional long-period seismic waveforms. This supports that the mechanism of submarine trapdoor faulting in Kita-Ioto caldera, which follows recent findings in Sumisu and Curtis calderas. Repeating vertical-T CLVD earthquakes and another tsunami signal following the 2015 earthquake strongly suggest the recurrence of trapdoor faulting in Kita-Ioto caldera.

Our mechanical model enables us to infer the pre-seismic magma overpressure beneath the submarine caldera, through quantification of the trapdoor faulting size. Assuming a ring fault

623 with an arc length of 90° and a horizontal crack at a depth of 2 km in the crust as a main model
624 setting, we estimated that high pre-seismic magma overpressure over ~10 MPa caused the
625 trapdoor faulting event. The main results also showed that the co-seismic magma pressure
626 change drops by only 10–20 % of the pre-seismic magma overpressure, and the crack volume
627 increases by 0.0030 km^3. This indicates that trapdoor faulting relieves a critically high stress
628 state in the caldera but still keeps a high stress level even after the faulting event.

629 We emphasize that the model outputs vary from half to twice, depending on model
630 setting, such as a ring-fault geometry or a crack depth. For example, a longer ring fault requires
631 less magma overpressure to generate the similar-sized tsunami but more effectively reduces the
632 overpressure, while larger magma overpressure is estimated when the source has a crack at a
633 deeper depth. Although these uncertainties were not solved from our limited dataset, or a single
634 tsunami record, the significant variations suggest that magmatic systems beneath calderas can be
635 strongly influenced by source properties of trapdoor faulting. Therefore, it is critical to study
636 trapdoor faulting in active calderas and its source properties for more robust estimation of
637 magma overpressure or stress states and for comprehensive understanding of behaviors of
638 inflating calderas.

639 **Acknowledgments**

640 We thank Kurama Okubo for helpful discussion. This study is funded by the JSPS
641 KAKENHI (Grant numbers JP20J01689).

642 **Data availability**

643 OBP data of DART system is available from DART® Bottom Pressure Recorder Data
644 Inventory of National Oceanic and Atmospheric Administration (National Oceanic and
645 Atmospheric Administration. 2005; https://www.ngdc.noaa.gov/hazard/dart/). Bathymetric data
646 of M7000 Digital Bathymetric Chart and JTOPO30 are available from the Japan Hydrographic
647 Association (https://www.jha.or.jp/shop/index.php?main_page=index). F-net seismic data of F-
648 net are available from the NIED (National Research Institute for Earth Science and Disaster
649 Resilience, 2019) (https://www.fnet.bosai.go.jp/top.php?LANG=en), and Global Seismograph
650 Network data are available through the IRIS Wilber 3 system (https://ds.iris.edu/wilber3/) or
651 IRIS Web Services (https://service.iris.edu/), including networks coded as IU and II (Global

Seismograph Network: GSN) (Albuquerque Seismological Laboratory/USGS, 2014; Scripps Institution of Oceanography, 1986), and IC (New China Digital Seismograph Network: NCDSN) (Albuquerque Seismological Laboratory (ASL)/USGS, 1992). The earthquake information is available from the GCMT catalog (https://www.globalcmt.org/). The Geoware TTT software (http://www.geoware-online.com/tsunami.html) is used for estimating tsunami arrival times. Focal mechanisms representing moment tensors are plotted with a MATLAB code developed by James Conder (available from https://www.mathworks.com/matlabcentral/fileexchange/61227-focalmech-fm-centerx-centery-diam-varargin). The data of the source model proposed for main results in this study (Figure 3) can be obtained from an open-access repository of Zenodo (https://doi.org/10.5281/zenodo.8344070).

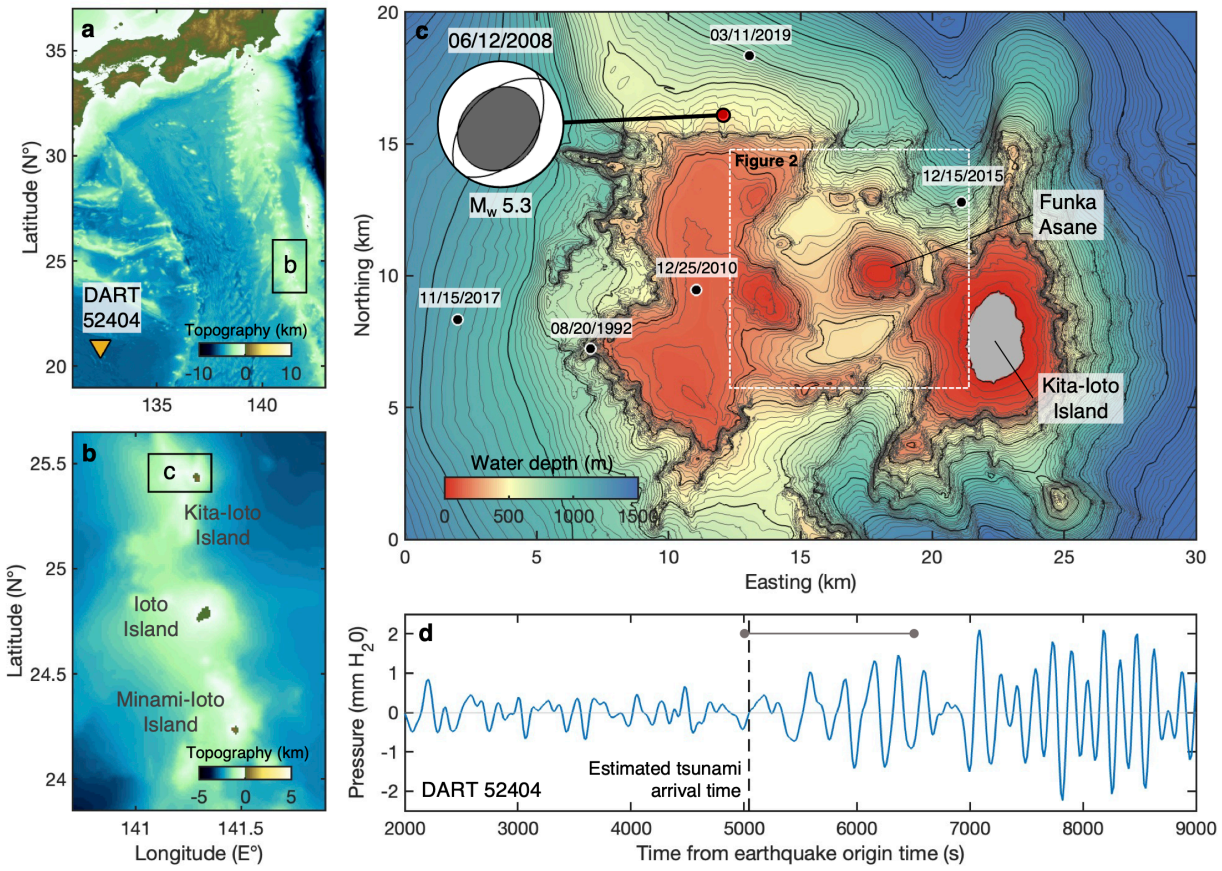

Figure 1. Vertical-T CLVD earthquakes near Kita-Ioto caldera. (**a**) Map of the southern ocean of Japan. Orange triangle represents the ocean-bottom-pressure (OBP) gauge of DART 52404. (**b**) Map of the region near Kita-Ioto Island. (**c**) Bathymetry of the region near Kita-Ioto caldera, a submarine caldera with a size of 12 km x 8 km, near Kita-Ioto Island. Funka Asane is the summit of a cone structure within the caldera rim. Red circle represents the location of the 2008 Kita-Ioto earthquake with its moment tensor, whereas black circles represent locations of similar events; the earthquake information is from the GCMT catalog (Ekström et al., 2012). The focal mechanism is shown as projections of the lower focal hemisphere, and the orientation of the best double-couple solution is shown by thin lines. (**d**) Tsunami waveform recorded at the OBP gauge of DART 52404. Dashed gray line represents the tsunami arrival time estimated using the Geoware TTT software. Solid gray line represents the data length for calculating the root-mean-square (RMS) amplitudes (Equation 14). This waveform data is obtained by removing the tidal trend from and by applying the bandpass (2–10 mHz) Butterworth filter to the raw OBP data for

677 12,000 s after the earthquake origin time. Note that oscillations of OBP changes with a few mm
678 H_2O are recorded after the estimated arrival time, indicating tsunami signals.
679

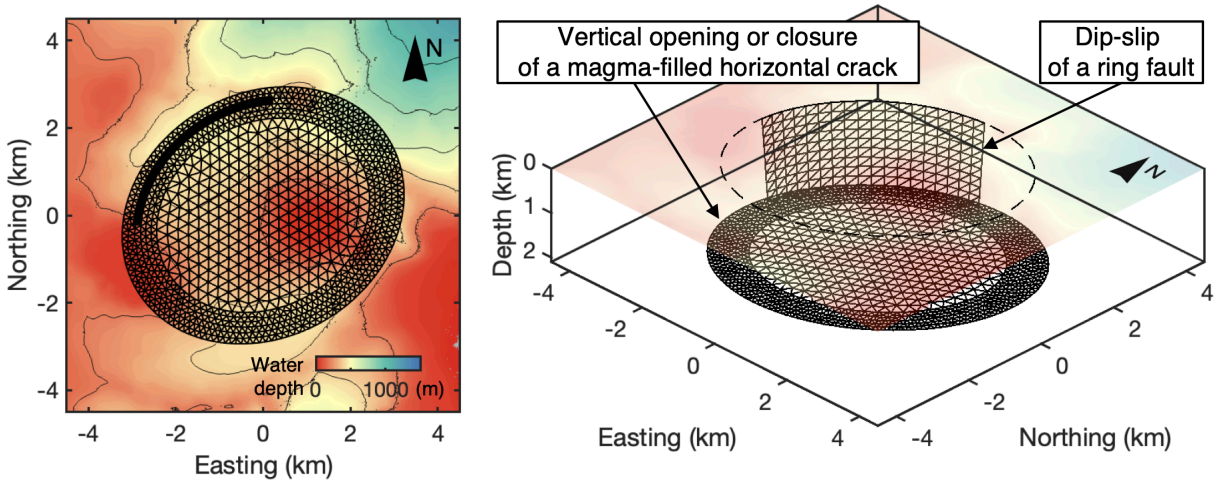

680

681 **Figure 2**. A source structure for the mechanical model of trapdoor faulting viewed from top
682 (left) and southeast (right). Gray lines are plotted every water depth of 200 m.

683

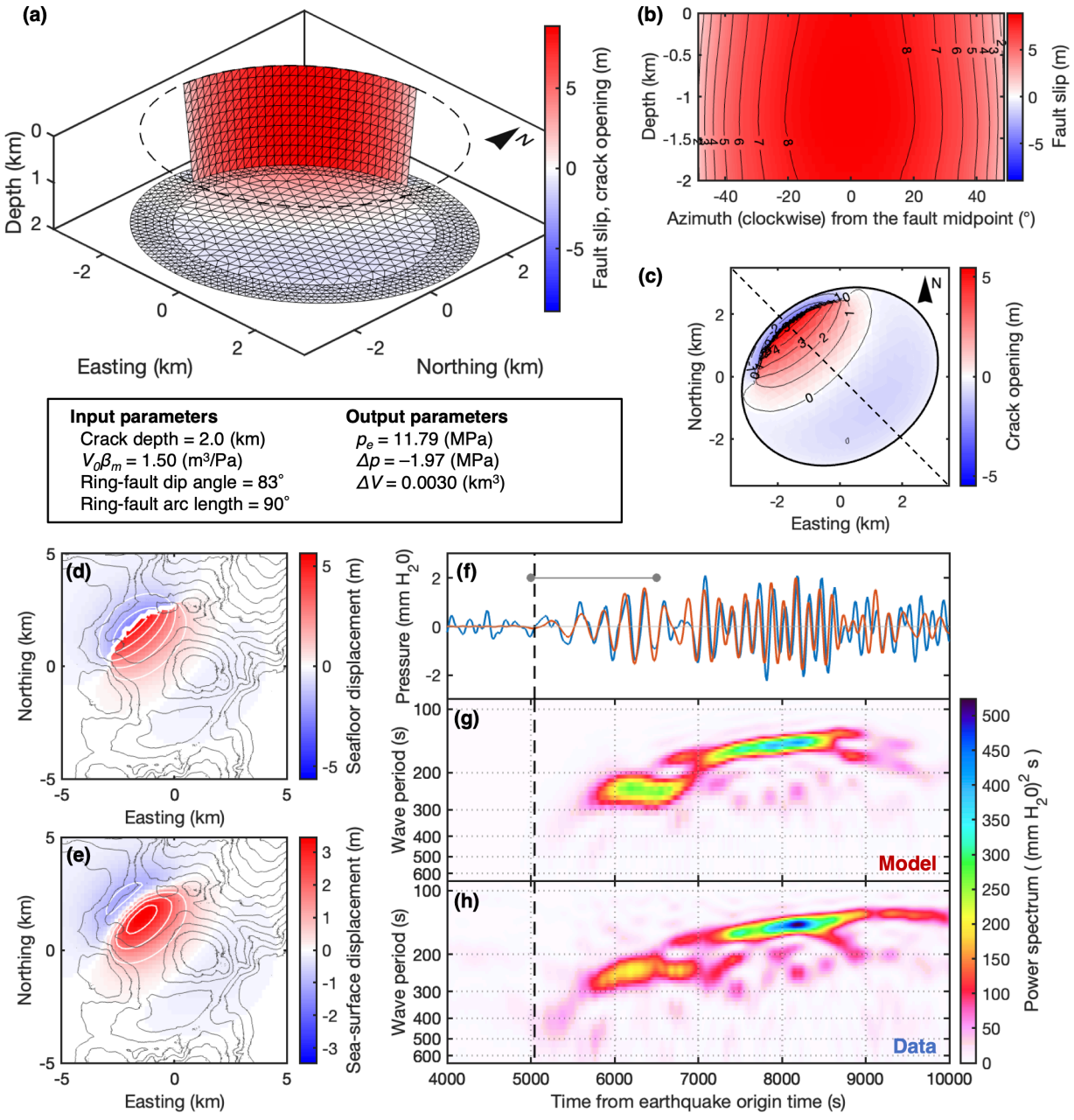

Figure 3. Mechanical trapdoor faulting model of the 2008 Kita-Ioto earthquake. (**a**) Mechanical model viewed from southeast, represented by dip slip of the ring fault $\underline{s}$ and vertical deformation of the crack $\underline{\delta}$. Red color on the ring fault represents reverse slip, while red and blue colors on the horizontal crack represent vertical opening and closure, respectively. (**b** and **c**) Spatial distributions of (**b**) the ring fault and (**c**) the horizontal crack. In **b**, the fault is viewed from the caldera center, and the azimuth from the caldera center to arbitrary point on the fault is measured clockwise from the midpoint of the fault. In **c**, dashed line represents a profile shown in Figure 5.

692 (**d** and **e**) Vertical displacement of seafloor (**d**) and sea surface (**e**) due to the model. Red and
693 blue colors represent uplift and subsidence, respectively, with white lines plotted every 1.0 m.
694 Black lines represent water depth every 100 m. (**f**) Comparison between a synthetic tsunami
695 waveform from the model (red line) and the observed OBP waveform (blue line) at the station
696 52404. Solid gray line represents the data length for calculating the root-mean-square (RMS)
697 amplitudes (Equation 14). (**g** and **h**) Spectrograms of the (**g**) synthetic and (**h**) observed
698 waveforms. In **f**–**h**, black dashed line represents the tsunami arrival time.

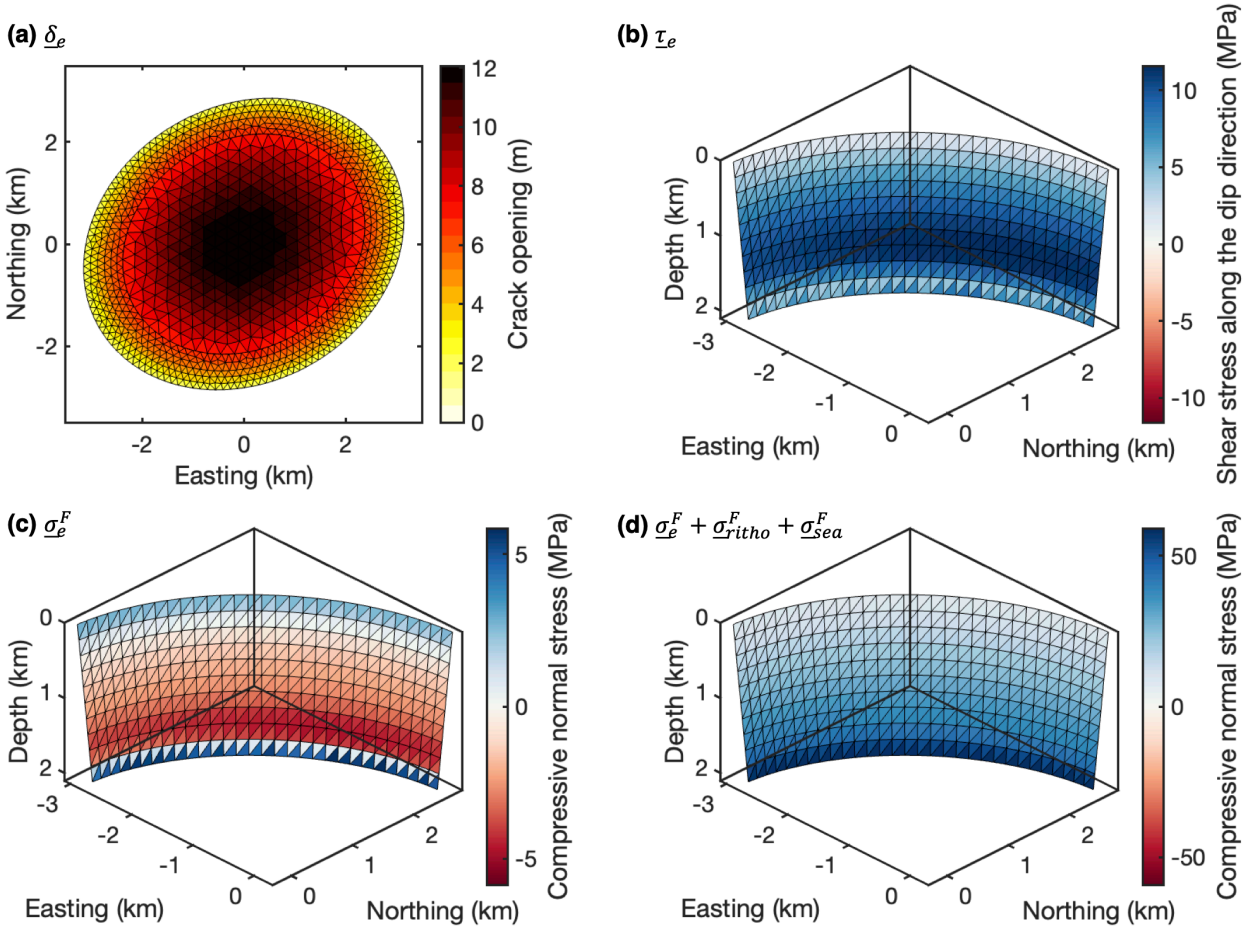

Figure 4. Critical status of the fault-crack system just before trapdoor faulting. (**a**) Distribution of the crack opening, $\underline{\delta_e}$. (**b**) Critical shear stress along dip-slip direction on the ring fault, $\underline{\tau_e}$. (**c**) Normal stress on the ring fault induced by the critically opening crack, $\underline{\sigma_e^F}$. In **b** and **c**, blue and red colors represent compressive and extensional normal stress, respectively. (**d**) Total normal stress on the ring fault, $\sigma_0^F = \sigma_e^F + \sigma_{lit}^F + \sigma_{sea}^F$; here, $\sigma_{lit}^F = \rho_h D_h g$, where ρ_h, D_h, and g are the host rock density (2,600 kg/m^3), the depth of each mesh, and the gravitational acceleration (9.81 m/s^2), respectively, and $\sigma_{sea}^F = \rho_s D_s g$, where ρ_s and D_s are the density and the averaged depth of the overlying seawater (1,020 kg/m^3 and 400 m), respectively.

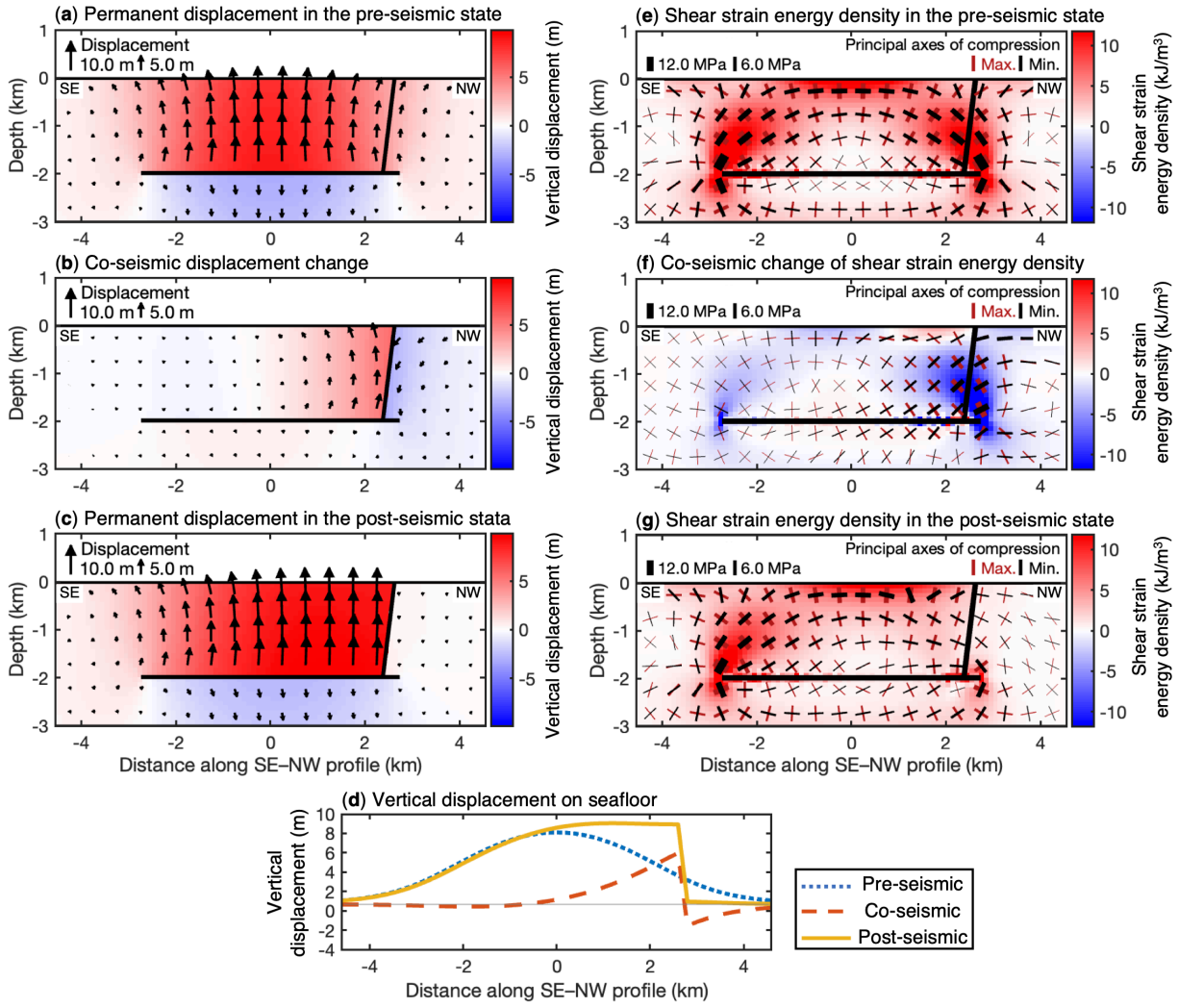

Figure 5. Displacement and shear-strain energy density in the host rock, along a SE–NW profile shown in Figure 3c. (**a**–**c**) Displacement, relative to the reference state ($p = p_0$): (**a**) the pre-seismic state just before trapdoor faulting, (**b**) the co-seismic change due to trapdoor faulting, and (**c**) the post-seismic state after trapdoor faulting. (**d**) Vertical seafloor displacement in each state shown in **a**, **b**, and **c**. (**e**–**g**) Shear-strain energy density W: (**e**) the pre-seismic state, (**f**) the co-seismic change, and (**g**) the post-seismic state. Color represents shear-strain energy density, and bars represent principal axes of compression projected on the profile, whose thickness reflects half the differential stress change $(\sigma_1 - \sigma_3)/2$, where σ_1 and σ_3 are the maximum and minimum stress, respectively.

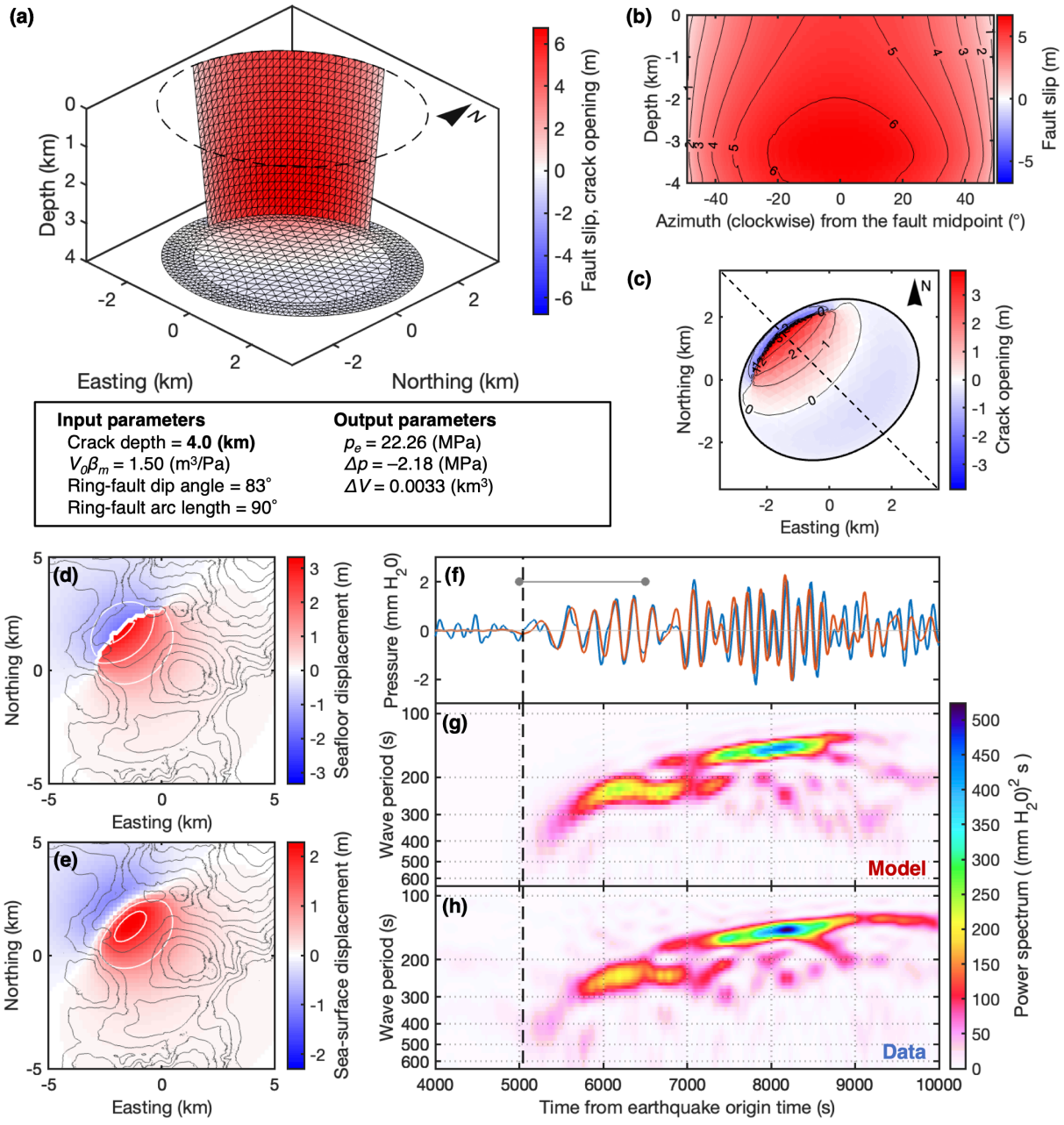

720

721 **Figure 6**. Same as Figure 3, but for a model with a horizontal crack at a depth of 4 km. See
722 details in Section 6.1.1.

723

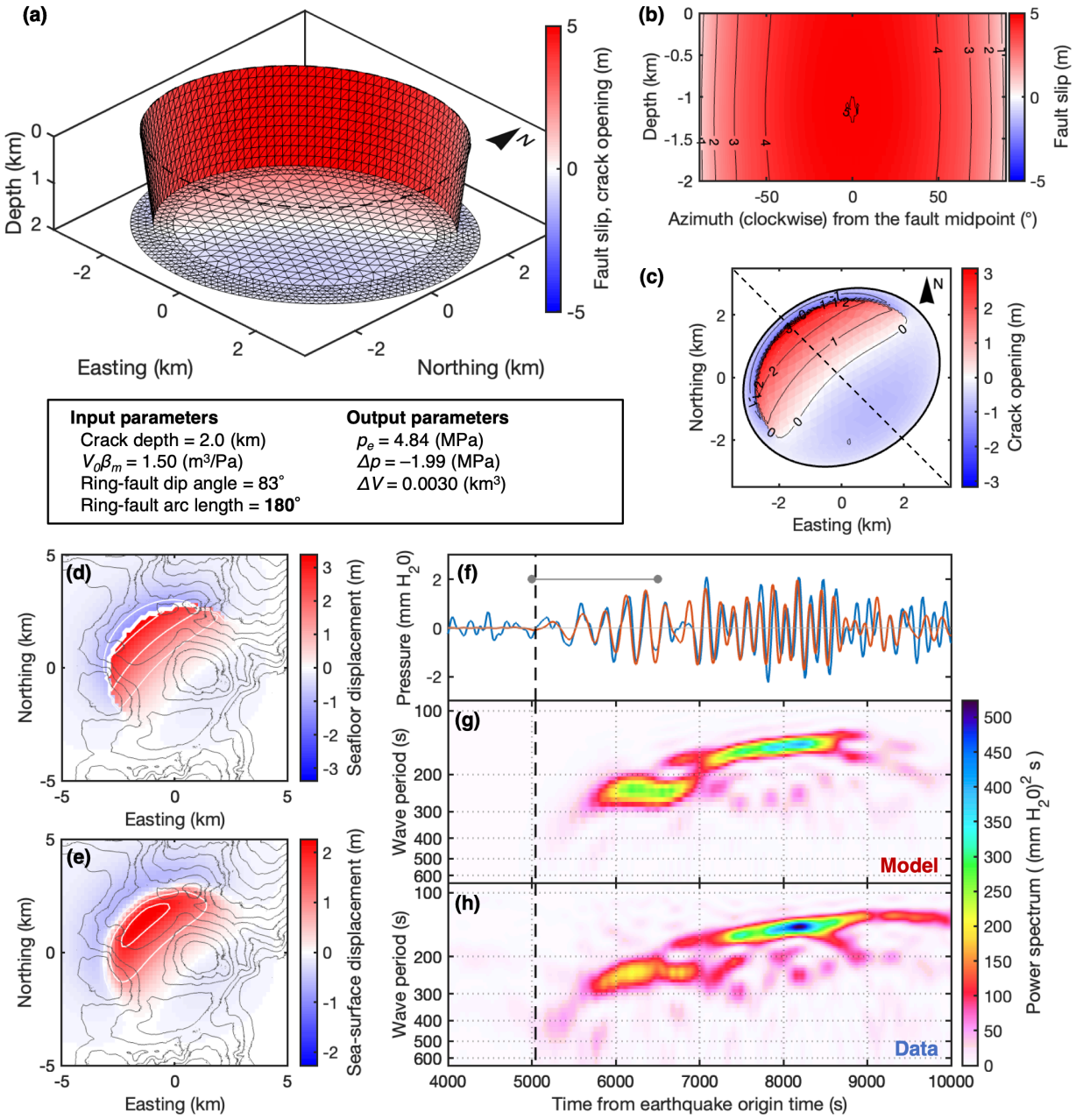

724

725 **Figure 7**. Same as Figure 3, but for a model with a longer ring fault of an arc ancle of 180°. See
726 details in Section 6.1.2.

727

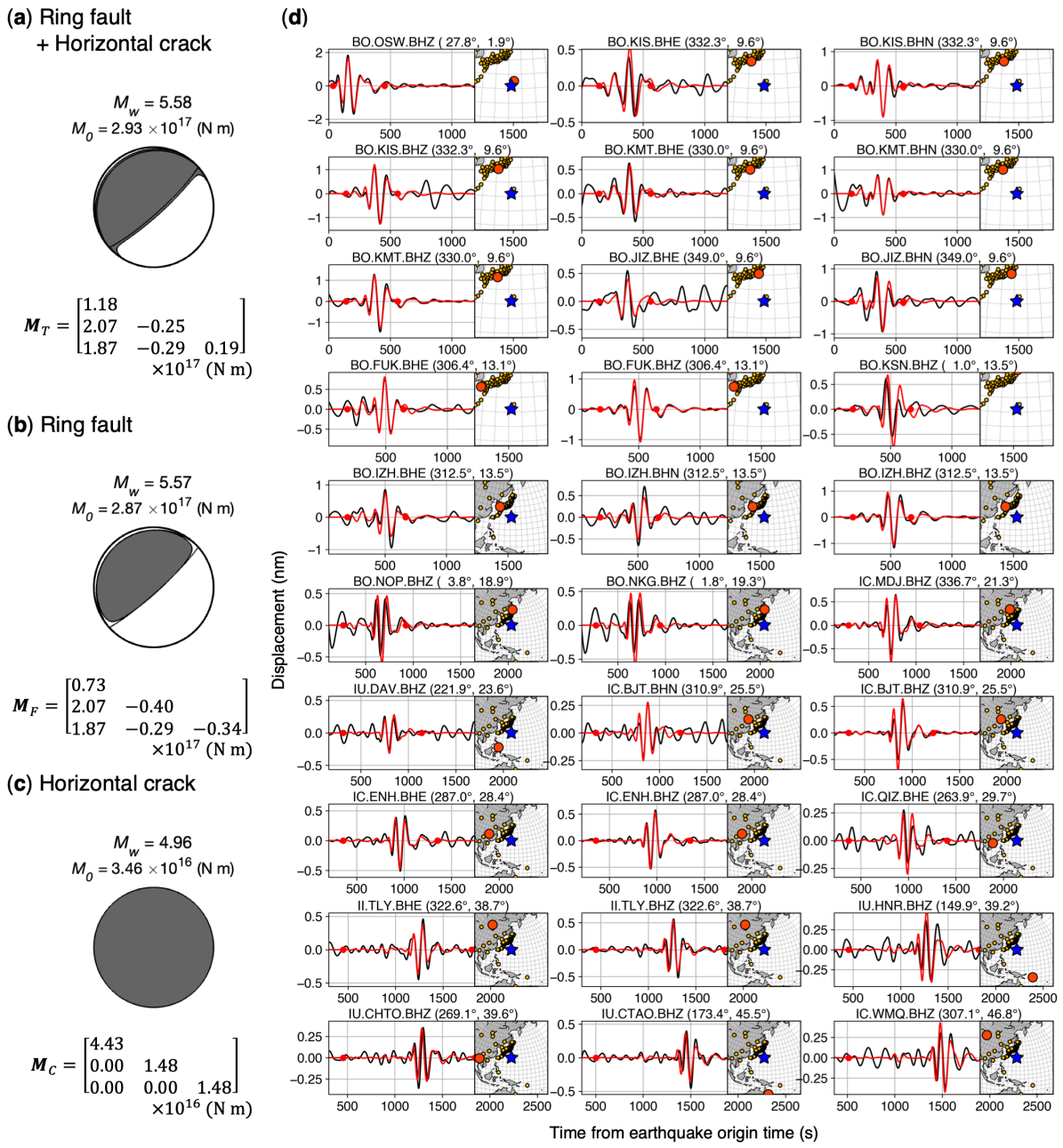

Figure 8. Long-period (80–200 s) seismic waveform modeling. (**a**) Moment tensor of the model, composed of partial moment tensors of (**b**) the ring fault and (**c**) the horizontal crack. (**d**) Comparison between synthetic waveforms (red line) and the observation (black line) at representative stations. In inset figures, a large red circle and a blue star represent the station and the earthquake centroid, respectively. On the top of each panel, the network name, station name, record component, station azimuth, and epicentral distance are shown. Note that waveform comparisons in all the tested seismic records are shown in Figure S8.

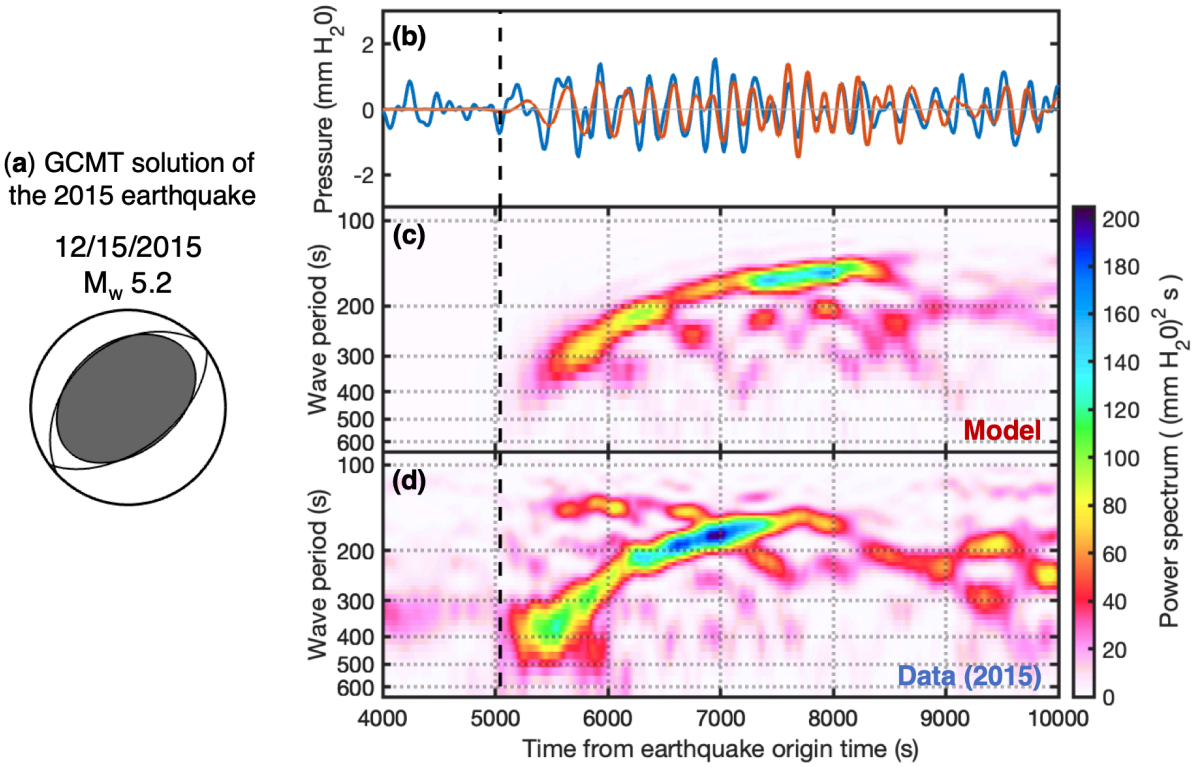

Figure 9. Tsunami waveform data from the 2015 earthquake. (**a**) The GCMT solution of the Kita-Ioto caldera earthquake on December 15, 2015. (**b**) Comparison between a synthetic tsunami waveform from a source model adjusted from the 2008 earthquake model (red line; see Section 6.4) and the observed OBP waveform (blue line) at the station 52404. (**c**–**d**) Spectrograms of the synthetic waveform (**c**) and the OBP waveform (**d**). In **b**–**d**, black dashed line represents the tsunami arrival time. Note that the location of the 52404 station as of the 2015 earthquake has been shifted by ~20 km southward from the location as of the 2008 earthquake (see text and Figure S6).

References

Albuquerque Seismological Laboratory (ASL)/USGS. (1992). IC: New China Digital Seismograph Network. https://doi.org/10.7914/SN/IC

Albuquerque Seismological Laboratory/USGS. (2014). IU: Global Seismograph Network (GSN - IRIS/USGS). https://doi.org/10.7914/SN/IU

Amelung, F., Jónsson, S., Zebker, H., & Segall, P. (2000). Widespread uplift and 'trapdoor' faulting on Galápagos volcanoes observed with radar interferometry. *Nature*, *407*(6807), 993–996. https://doi.org/10.1038/35039604

Anderson, K. R., Johanson, I. A., Patrick, M. R., Gu, M., Segall, P., Poland, M. P., et al. (2019). Magma reservoir failure and the onset of caldera collapse at Kīlauea Volcano in 2018. *Science*, *366*(6470). https://doi.org/10.1126/science.aaz1822

Baba, T., Takahashi, N., Kaneda, Y., Ando, K., Matsuoka, D., & Kato, T. (2015). Parallel Implementation of Dispersive Tsunami Wave Modeling with a Nesting Algorithm for the 2011 Tohoku Tsunami. *Pure and Applied Geophysics*, *172*(12), 3455–3472. https://doi.org/10.1007/s00024-015-1049-2

Bell, A. F., Hernandez, S., La Femina, P. C., & Ruiz, M. C. (2021). Uplift and seismicity driven by magmatic inflation at Sierra Negra volcano, Galápagos islands. *Journal of Geophysical Research, [Solid Earth]*, *126*(7). https://doi.org/10.1029/2021jb022244

Bernard, E. N., & Meinig, C. (2011). History and future of deep-ocean tsunami measurements. In *OCEANS'11 MTS/IEEE KONA* (pp. 1–7). ieeexplore.ieee.org. https://doi.org/10.23919/OCEANS.2011.6106894

Cabaniss, H. E., Gregg, P. M., Nooner, S. L., & Chadwick, W. W., Jr. (2020). Triggering of eruptions at Axial Seamount, Juan de Fuca Ridge. *Scientific Reports*, *10*(1), 10219. https://doi.org/10.1038/s41598-020-67043-0

Cesca, S., Letort, J., Razafindrakoto, H. N. T., Heimann, S., Rivalta, E., Isken, M. P., et al. (2020). Drainage of a deep magma reservoir near Mayotte inferred from seismicity and deformation. *Nature Geoscience*, *13*(1), 87–93. https://doi.org/10.1038/s41561-019-0505-5

Chikasada, N. Y. (2019). Short-wavelength Tsunami Observation Using Deep Ocean Bottom Pressure Gauges. In *The 29th International Ocean and Polar Engineering Conference*.

776 International Society of Offshore and Polar Engineers. Retrieved from
777 https://onepetro.org/conference-paper/ISOPE-I-19-707
778 Cole, J. W., Milner, D. M., & Spinks, K. D. (2005). Calderas and caldera structures: a review.
779 *Earth-Science Reviews*, *69*(1), 1–26. https://doi.org/10.1016/j.earscirev.2004.06.004
780 Duputel, Z., Rivera, L., Kanamori, H., & Hayes, G. (2012). W phase source inversion for
781 moderate to large earthquakes (1990–2010). *Geophysical Journal International*, *189*(2),
782 1125–1147. https://doi.org/10.1111/j.1365-246X.2012.05419.x
783 Ekström, G., Nettles, M., & Dziewoński, A. M. (2012). The global CMT project 2004–2010:
784 Centroid-moment tensors for 13,017 earthquakes. *Physics of the Earth and Planetary*
785 *Interiors*, *200-201*, 1–9. https://doi.org/10.1016/j.pepi.2012.04.002
786 Eshelby, J. D. (1957). The Determination of the Elastic Field of an Ellipsoidal Inclusion, and
787 Related Problems. *Proceedings of the Royal Society of London. Series A, Mathematical*
788 *and Physical Sciences*, *241*(1226), 376–396. Retrieved from
789 http://www.jstor.org/stable/100095
790 Fukao, Y., Sandanbata, O., Sugioka, H., Ito, A., Shiobara, H., Watada, S., & Satake, K. (2018).
791 Mechanism of the 2015 volcanic tsunami earthquake near Torishima, Japan. *Science*
792 *Advances*, *4*(4), eaao0219. https://doi.org/10.1126/sciadv.aao0219
793 Geist, D. J., Harpp, K. S., Naumann, T. R., Poland, M., Chadwick, W. W., Hall, M., & Rader, E.
794 (2008). The 2005 eruption of Sierra Negra volcano, Galápagos, Ecuador. *Bulletin of*
795 *Volcanology*, *70*(6), 655–673. https://doi.org/10.1007/s00445-007-0160-3
796 Gregg, P. M., Le Mével, H., Zhan, Y., Dufek, J., Geist, D., & Chadwick, W. W., Jr. (2018).
797 Stress triggering of the 2005 eruption of Sierra Negra volcano, Galápagos. *Geophysical*
798 *Research Letters*, *45*(24), 13288–13297. https://doi.org/10.1029/2018gl080393
799 Gregg, P. M., Zhan, Y., Amelung, F., Geist, D., Mothes, P., Koric, S., & Yunjun, Z. (2022).
800 Forecasting mechanical failure and the 26 June 2018 eruption of Sierra Negra Volcano,
801 Galápagos, Ecuador. *Science Advances*, *8*(22), eabm4261.
802 https://doi.org/10.1126/sciadv.abm4261
803 Grilli, S. T., Tappin, D. R., Carey, S., Watt, S. F. L., Ward, S. N., Grilli, A. R., et al. (2019).
804 Modelling of the tsunami from the December 22, 2018 lateral collapse of Anak Krakatau
805 volcano in the Sunda Straits, Indonesia. *Scientific Reports*, *9*(1), 11946.
806 https://doi.org/10.1038/s41598-019-48327-6

807 Hardebeck, J. L., & Okada, T. (2018). Temporal stress changes caused by earthquakes: A
808 review. *Journal of Geophysical Research, [Solid Earth]*, *123*(2), 1350–1365.
809 https://doi.org/10.1002/2017jb014617
810 Hasegawa, A., Yoshida, K., & Okada, T. (2011). Nearly complete stress drop in the 2011 Mw
811 9.0 off the Pacific coast of Tohoku Earthquake. *Earth, Planets and Space*, *63*(7), 35.
812 https://doi.org/10.5047/eps.2011.06.007
813 Hayes, G. P., Rivera, L., & Kanamori, H. (2009). Source Inversion of the W-Phase: Real-time
814 Implementation and Extension to Low Magnitudes. *Seismological Research Letters*,
815 *80*(5), 817‑822. https://doi.org/10.1785/gssrl.80.5.817
816 Heidarzadeh, M., Ishibe, T., Sandanbata, O., Muhari, A., & Wijanarto, A. B. (2020). Numerical
817 modeling of the subaerial landslide source of the 22 December 2018 Anak Krakatoa
818 volcanic tsunami, Indonesia. *Ocean Engineering*, *195*, 106733.
819 https://doi.org/10.1016/j.oceaneng.2019.106733
820 Jónsson, S. (2009). Stress interaction between magma accumulation and trapdoor faulting on
821 Sierra Negra volcano, Galápagos. *Tectonophysics*, *471*(1), 36–44.
822 https://doi.org/10.1016/j.tecto.2008.08.005
823 Kajiura, K. (1963). The Leading Wave of a Tsunami. *Bulletin of the Earthquake Research*
824 *Institute, University of Tokyo*, *41*(3), 535–571. Retrieved from
825 https://ci.nii.ac.jp/naid/120000866529/
826 Kanamori, H., & Rivera, L. (2008). Source inversion of Wphase: speeding up seismic tsunami
827 warning. *Geophysical Journal International*, *175*(1), 222–238.
828 https://doi.org/10.1111/j.1365-246X.2008.03887.x
829 Kilbride, B. M., Edmonds, M., & Biggs, J. (2016). Observing eruptions of gas-rich compressible
830 magmas from space. *Nature Communications*, *7*, 13744.
831 https://doi.org/10.1038/ncomms13744
832 Kubota, T., Saito, T., & Nishida, K. (2022). Global fast-traveling tsunamis by atmospheric
833 pressure waves on the 2022 Tonga eruption. Retrieved from
834 http://eartharxiv.org/repository/view/3090/
835 Lai, V. H., Zhan, Z., Brissaud, Q., Sandanbata, O., & Miller, M. S. (2021). Inflation and
836 asymmetric collapse at kīlauea summit during the 2018 eruption from seismic and

infrasound analyses. *Journal of Geophysical Research, [Solid Earth]*. https://doi.org/10.1029/2021jb022139

Le Mével, H., Gregg, P. M., & Feigl, K. L. (2016). Magma injection into a long-lived reservoir to explain geodetically measured uplift: Application to the 2007-2014 unrest episode at Laguna del Maule volcanic field, Chile. *Journal of Geophysical Research, [Solid Earth]*, *121*(8), 6092–6108. https://doi.org/10.1002/2016JB013066

Lynett, P., McCann, M., Zhou, Z., Renteria, W., Borrero, J., Greer, D., et al. (2022). Diverse tsunamigenesis triggered by the Hunga Tonga-Hunga Ha'apai eruption. *Nature*, *609*(7928), 728–733. https://doi.org/10.1038/s41586-022-05170-6

Massa, B., D'Auria, L., Cristiano, E., & De Matteo, A. (2016). Determining the Stress Field in Active Volcanoes Using Focal Mechanisms. *Frontiers of Earth Science in China*, *4*. https://doi.org/10.3389/feart.2016.00103

Metz, D., Watts, A. B., Grevemeyer, I., Rodgers, M., & Paulatto, M. (2016). Ultra‐long‐range hydroacoustic observations of submarine volcanic activity at Monowai, Kermadec Arc. *Geophysical Research Letters*, *43*(4), 1529–1536. https://doi.org/10.1002/2015gl067259

Moyer, P. A., Boettcher, M. S., Bohnenstiehl, D. R., & Abercrombie, R. E. (2020). Crustal strength variations inferred from earthquake stress drop at axial seamount surrounding the 2015 eruption. *Geophysical Research Letters*, *47*(16). https://doi.org/10.1029/2020gl088447

National Research Institute for Earth Science and Disaster Resilience. (2019). NIED F-net [Data set]. National Research Institute for Earth Science and Disaster Resilience. https://doi.org/10.17598/NIED.0005

Nikkhoo, M., & Walter, T. R. (2015). Triangular dislocation: an analytical, artefact-free solution. *Geophysical Journal International*, *201*(2), 1119–1141. https://doi.org/10.1093/gji/ggv035

Purkis, S. J., Ward, S. N., Fitzpatrick, N. M., Garvin, J. B., Slayback, D., Cronin, S. J., et al. (2023). The 2022 Hunga-Tonga megatsunami: Near-field simulation of a once-in-a-century event. *Science Advances*, *9*(15), eadf5493. https://doi.org/10.1126/sciadv.adf5493

Ross, Z. E., Kanamori, H., & Hauksson, E. (2017). Anomalously large complete stress drop during the 2016M_w5.2 Borrego Springs earthquake inferred by waveform modeling and

near‐source aftershock deficit. *Geophysical Research Letters*, *44*(12), 5994–6001. https://doi.org/10.1002/2017gl073338

Saito, T., Matsuzawa, T., Obara, K., & Baba, T. (2010). Dispersive tsunami of the 2010 Chile earthquake recorded by the high-sampling-rate ocean-bottom pressure gauges. *Geophysical Research Letters*, *37*(23). https://doi.org/10.1029/2010gl045290

Saito, T., Noda, A., Yoshida, K., & Tanaka, S. (2018). Shear strain energy change caused by the interplate coupling along the Nankai trough: An integration analysis using stress tensor inversion and slip-deficit inversion. *Journal of Geophysical Research, [Solid Earth]*, *123*(7), 5975–5986. https://doi.org/10.1029/2018jb015839

Sandanbata, O., Watada, S., Satake, K., Fukao, Y., Sugioka, H., Ito, A., & Shiobara, H. (2018). Ray Tracing for Dispersive Tsunamis and Source Amplitude Estimation Based on Green's Law: Application to the 2015 Volcanic Tsunami Earthquake Near Torishima, South of Japan. *Pure and Applied Geophysics*, *175*(4), 1371–1385. https://doi.org/10.1007/s00024-017-1746-0

Sandanbata, O., Kanamori, H., Rivera, L., Zhan, Z., Watada, S., & Satake, K. (2021). Moment tensors of ring‐faulting at active volcanoes: Insights into vertical‐CLVD earthquakes at the Sierra Negra caldera, Galápagos islands. *Journal of Geophysical Research, [Solid Earth]*, *126*(6), e2021JB021693. https://doi.org/10.1029/2021jb021693

Sandanbata, O., Watada, S., Ho, T.-C., & Satake, K. (2021). Phase delay of short-period tsunamis in the density-stratified compressible ocean over the elastic Earth. *Geophysical Journal International*, *226*(3), 1975–1985. https://doi.org/10.1093/gji/ggab192

Sandanbata, O., Watada, S., Satake, K., Kanamori, H., Rivera, L., & Zhan, Z. (2022). Sub‐decadal volcanic tsunamis due to submarine trapdoor faulting at sumisu caldera in the Izu–Bonin arc. *Journal of Geophysical Research, [Solid Earth]*, *127*(9). https://doi.org/10.1029/2022jb024213

Sandanbata, O., Watada, S., Satake, K., Kanamori, H., & Rivera, L. (2023). Two volcanic tsunami events caused by trapdoor faulting at a submerged caldera near Curtis and Cheeseman islands in the kermadec arc. *Geophysical Research Letters*, *50*(7). https://doi.org/10.1029/2022gl101086

Saurel, J.-M., Jacques, E., Aiken, C., Lemoine, A., Retailleau, L., Lavayssière, A., et al. (2021). Mayotte seismic crisis: building knowledge in near real-time by combining land and

ocean-bottom seismometers, first results. *Geophysical Journal International*, *228*(2), 1281–1293. https://doi.org/10.1093/gji/ggab392

Scripps Institution of Oceanography. (1986). II: Global Seismograph Network - IRIS/IDA. https://doi.org/10.7914/SN/II

Segall, P., & Anderson, K. (2021). Repeating caldera collapse events constrain fault friction at the kilometer scale. *Proceedings of the National Academy of Sciences of the United States of America*, *118*(30). https://doi.org/10.1073/pnas.2101469118

Shelly, D. R., & Thelen, W. A. (2019). Anatomy of a caldera collapse: Kīlauea 2018 summit seismicity sequence in high resolution. *Geophysical Research Letters*, *46*(24), 14395–14403. https://doi.org/10.1029/2019gl085636

Shreve, T., & Delgado, F. (2023). Trapdoor fault activation: A step towards caldera collapse at Sierra Negra, Galápagos, Ecuador. *Journal of Geophysical Research, [Solid Earth]*. https://doi.org/10.1029/2023jb026437

Sparks, R. S. J. (2003). Forecasting volcanic eruptions. *Earth and Planetary Science Letters*, *210*(1), 1–15. https://doi.org/10.1016/S0012-821X(03)00124-9

Sugioka, H., Fukao, Y., Okamoto, T., & Kanjo, K. (2001). Detection of shallowest submarine seismicity by acoustic coupled shear waves. *Journal of Geophysical Research*, *106*(B7), 13485–13499. https://doi.org/10.1029/2000jb900476

Tepp, G., & Dziak, R. P. (2021). The Seismo-Acoustics of Submarine Volcanic Eruptions. *Journal of Geophysical Research, [Solid Earth]*, *126*(4), e2020JB020912. https://doi.org/10.1029/2020JB020912

Wang, T. A., Coppess, K. R., Segall, P., Dunham, E. M., & Ellsworth, W. (2022). Physics‐based model reconciles caldera collapse induced static and dynamic ground motion: Application to kīlauea 2018. *Geophysical Research Letters*, *49*(8). https://doi.org/10.1029/2021gl097440

Wang, T. A., Segall, P., Hotovec-Ellis, A. J., Anderson, K. R., & Cervelli, P. F. (2023). Ring fault creep drives volcano-tectonic seismicity during caldera collapse of Kīlauea in 2018. *Earth and Planetary Science Letters*, *618*, 118288. https://doi.org/10.1016/j.epsl.2023.118288

Wang, Y., Satake, K., Sandanbata, O., Maeda, T., & Su, H. (2019). Tsunami data assimilation of cabled ocean bottom pressure records for the 2015 torishima volcanic tsunami

earthquake. *Journal of Geophysical Research, [Solid Earth]*, *124*(10), 10413–10422. https://doi.org/10.1029/2019jb018056

Wells, D. L., & Coppersmith, K. J. (1994). New Empirical Relationships among Magnitude, Rupture Length, Rupture Width, Rupture Area, and Surface Displacement. *Bulletin of the Seismological Society of America*, *84*(4), 974–1002. https://doi.org/10.1785/BSSA0840040974

Ye, L., Kanamori, H., Rivera, L., Lay, T., Zhou, Y., Sianipar, D., & Satake, K. (2020). The 22 December 2018 tsunami from flank collapse of Anak Krakatau volcano during eruption. *Science Advances*, *6*(3), eaaz1377. https://doi.org/10.1126/sciadv.aaz1377

Zhan, Y., & Gregg, P. M. (2019). How accurately can we model magma reservoir failure with uncertainties in host rock rheology? *Journal of Geophysical Research, [Solid Earth]*, *124*(8), 8030–8042. https://doi.org/10.1029/2019jb018178

Zheng, Y., Blackstone, L., & Segall, P. (2022). Constraints on absolute magma chamber volume from geodetic measurements of trapdoor faulting at Sierra Negra volcano, Galapagos. *Geophysical Research Letters*, *49*(5). https://doi.org/10.1029/2021gl095683

References From the Supporting Information

Aki, K., & Richards, P. G. (1980). *Quantitative seismology: theory and methods* (Vol. 842). Freeman San Francisco, CA.

Dziewonski, A. M., & Anderson, D. L. (1981). Preliminary reference Earth model. *Physics of the Earth and Planetary Interiors*, *25*(4), 297–356. https://doi.org/10.1016/0031-9201(81)90046-7

Kawakatsu, H., & Yamamoto, M. (2015). 4.15 - Volcano Seismology. In G. Schubert (Ed.), *Treatise on Geophysics (Second Edition)* (pp. 389–419). Oxford: Elsevier. https://doi.org/10.1016/B978-0-444-53802-4.00081-6

Takeuchi, H., & Saito, M. (1972). Seismic surface waves. *Methods in Computational Physics*, *11*, 217–295.